Separable downmodulation of meiotic axis protein deposition and DNA break induction at chromosome ends

Adhithi R. Raghavan[1], Kieron May[2], Vijayalakshmi V. Subramanian[1,3], Hannah G. Blitzblau[1], Neem J. Patel[1], Jonathan Houseley[2], Andreas Hochwagen[1*]

Affiliations:

1. Department of Biology, New York University, New York, NY 10003, USA
2. Epigenetics Programme, Babraham Institute, Cambridge, CB22 3AT, UK
3. Department of Biology, IISER Tirupati, Tirupati, 517507, Andhra Pradesh, India

*Corresponding Author (andi@nyu.edu)

Abstract:

In many organisms, meiotic crossover recombination is suppressed near the extreme ends of chromosomes. Here we show that multiple, often chromosome-specific, suppressive mechanisms with differing ranges contribute to the consistently low enrichment of recombination-promoting axis proteins and downregulation of DNA double-strand breaks (DSBs) within 20 kb of telomeres in *Saccharomyces cerevisiae*. Suppression of axis proteins is associated with *cis*-encoded signals and correlates with reduced coding density, although whether this sequence feature actively drives suppression remains to be determined. In addition, axis protein suppression requires the histone methyltransferase Dot1 and the Sir silencing complex. We show that Dot1 suppresses Sir complex activity at least in part independently of its canonical target, H3K79, to downmodulate axis protein deposition near chromosome ends. In parallel, the Sir complex, but not Dot1, suppresses the induction of DSBs at a small number of cryptic hotspots by limiting the openness of promoters, the preferred sites of meiotic DSB formation. Much of the reduced DSB induction near chromosome ends persists in *dot1* and *sir3* mutants, indicating that additional layers of regulation contribute to the robust reduction of meiotic recombination effectors near chromosome ends.

Keywords: meiotic DSBs, subtelomeres, axis proteins, chromatin modifiers, Dot1, Sir2, Sir3

30 **Introduction:**

31 Meiosis is a specialized type of cell division that generates haploid gametes from diploid
32 progenitor cells and plays an essential role in promoting genetic diversity [1]. Meiosis begins with a
33 single round of DNA replication followed by two rounds of chromosome segregation, first
34 segregating homologous chromosomes and then sister chromatids [2,3]. Accurate segregation
35 during meiosis I relies on meiotic crossover recombination, which exchanges DNA between
36 homologous chromosome pairs and, together with sister chromatid cohesion, forms a physical
37 connection between them [4]. Meiotic recombination is initiated by programmed DNA double-strand
38 breaks (DSBs), which are catalyzed by Spo11, a highly conserved topoisomerase-like enzyme [5].

39 Although DSBs can occur throughout the genome, their frequencies vary widely. Chromosomal
40 regions classified as "hot" experience frequent DSBs, whereas "cold" regions, including
41 centromeres and chromosome ends, rarely undergo breakage [6]. Hotness results from a complex
42 interplay of factors, including local base composition, chromatin modifications, meiotic
43 chromosome architecture, as well as environmental factors [5,7-9].

44 In addition to DSBs, the differential distribution of meiosis-specific axis proteins, which localize at
45 the base of the loop-axis structure of meiotic chromosomes, has a major impact on recombination
46 levels across the genome. Axis proteins can promote DSB activity and are also essential for
47 directing repair toward the homologous chromosome, and thus crossover formation [6,10-12]. In *S.*
48 *cerevisiae*, elevated binding of the axis proteins Red1 and Hop1 is often associated with markers
49 of crossover repair [13,14]. Red1 and Hop1 are recruited to the base of chromatin loops by the meiotic
50 Rec8-cohesin complex but can also bind directly to chromatin through the nucleosome-binding
51 activity of Hop1 [13,15,16], leading to two independent modes of axis protein-dependent patterning of
52 meiotic recombination.

53 In *S. cerevisiae*, levels of DSBs and crossover formation exhibit a distinctive pattern near
54 chromosome ends. Levels are elevated above genome average in the end-adjacent regions
55 (EARs), large chromosomal regions located 20-120 kb from chromosome ends, but notably
56 reduced within ~20 kb from telomeres [11,17-20]. The depletion within the last ~20 kb is likely
57 important for two reasons. First, these regions are enriched for repetitive DNA sequences that are
58 vulnerable to non-allelic homologous recombination (NAHR) and genome rearrangements [21].
59 Second, crossovers near chromosome ends are less effective at forming stable connections
60 between homologous chromosomes and may lead to chromosome mis-segregation if they are
61 the only connection between homolog pairs [22]. Consistent with this notion, recombination events
62 near telomeres are linked to a higher risk of Trisomy 21 (Down syndrome) in humans [23,24].

63 *S. cerevisiae* chromosome ends consist of several distinct genomic domains (**Fig. 1a**) [25,26],
64 including the telomerase-templated telomeric repeats that cap chromosome ends and the
65 "telomere-associated sequences", which contain repetitive Y' and X elements. In addition, the
66 "subtelomeric domains" extend inward for an average of about 20 kb from telomeres.
67 Subtelomeric domains are relatively gene-poor regions enriched in gene families [27,28]. In
68 vegetative cells, the telomeric repeats and X elements recruit the Sir2/Sir3/Sir4 histone
69 deacetylase complex, establishing transcriptional silencing. This silent chromatin can spread over
70 limited distances into the subtelomeric domains [29]. The subtelomeric domains, in turn, are defined
71 by a unique chromatin signature, which includes a relative depletion of active chromatin marks
72 [28,30]. Whether similar chromatin patterns exist during meiotic recombination is unknown.

73 Previous studies of meiotic recombination in *S. cerevisiae* have consistently shown a depletion of
74 DSBs in X and Y' elements as well as in the subtelomeric domains [11,17,31,32]. While the
75 mechanisms governing DSB suppression in X and Y' elements remain largely unexplored, the
76 reduced DSB levels in the subtelomeric domains are accompanied by lower recruitment of DSB-
77 promoting factors, such as Rec114 [33], and diminished abundance of Hop1 [19]. Hop1, which recruits

78 Rec114 [12], is currently the most upstream regulator of recombination known to be depleted within
79 ~20 kb from chromosome ends. Whether other axis proteins are similarly depleted and the
80 specific mechanisms controlling this altered distribution, as well as whether depletion is linked to
81 the suppression of meiotic DSBs is unknown.

82 **Results:**

83 **Axis protein enrichment patterns at chromosome ends**

84 Given the reduced axis protein enrichment near chromosome ends and their critical role in meiotic
85 DSB formation and repair, we investigated how axis proteins interact with telomere-associated
86 sequences and subtelomeric domains. These regions are often excluded from sequence-based
87 analyses due to variations in telomere organization even among closely related yeast strains
88 [25,34,35], and because the abundance of repetitive sequences and gene families creates challenges
89 for uniquely assigning sequencing reads. Therefore, we tailored our analysis pipeline to account
90 for these unique biological features. To reduce structural mapping artifacts, we mapped reads to
91 high-quality end-to-end chromosome scaffolds of our experimental strain (SK1) [35], rather than the
92 commonly used S288c reference. Although the inherent instability of subtelomeric domains
93 means that individual SK1 isolates may differ from the SK1 reference at some ends, this approach
94 eliminates the profound telomere-proximal sequence differences between SK1 and S288c as a
95 major source of error. Further, by exclusively considering optimal matches, we maximized the
96 number of confidently mapped reads, leveraging inherent sequence polymorphisms within
97 telomeric repeat sequences for unique mapping.

98 To validate our pipeline, we assessed mapping and coverage characteristics in unenriched input
99 datasets. Even in the highly repetitive X and Y' elements, our pipeline was able to uniquely map
100 12.8% and 0.87% of single-end reads and 15.2% and 12.8% of paired-end reads, respectively.
101 In the subtelomeric domains as a whole (within 20 kb from chromosome ends), unique mapping

102 rates were higher, averaging 24.1% for single-end reads and 32.2% for paired-end reads
103 (**Supplementary Fig. 1a**). In addition, we observed no systematic differences in fragmentation
104 efficiency (**Supplementary Fig. 1b**) and only minor differences in sequence coverage due to
105 incomplete X-element annotation (**Supplementary Fig. 1c**), indicating that telomere-proximal
106 regions are sampled comparably to the chromosome interior.

107 If a read had multiple equally good alignments, our pipeline randomly selected one location as
108 the primary alignment for the read. This approach did not affect metagene analyses but
109 significantly improved signal clarity at individual chromosome ends by closing coverage gaps
110 caused by a lack of polymorphisms. Comparative analysis of ChIP profiles with and without
111 multiple-mapping reads revealed no qualitative differences (**Supplementary Fig. 1d**).

112 Having validated our pipeline, we analyzed the distribution of axis proteins at chromosome ends
113 using previously published ChIP-seq datasets [16,19,36]. Meta-analysis showed that Hop1 was
114 depleted below genome average within 20 kb of chromosome ends and enriched above genome
115 average in the EARs (20-120 kb; **Fig. 1b-c**), consistent with previous studies [19]. This pattern was
116 mirrored by Red1, in line with the observation that Hop1 and Red1 depend on each other for
117 chromosomal association [16]. Axis protein depletion in the first 20 kb was observed across all
118 chromosome ends and thus could not be attributed to individual telomere outliers
119 (**Supplementary Fig. 2, 3a**).

120 Yeast chromosome ends are characterized by telomeric repeats, $(TG_{1-3})_n$, and telomere-
121 associated sequences, which include the Y' and X elements [37]. The long Y' elements (4-7 kb) are
122 not found on all ends and can occur as one or multiple copies, whereas a short X element (~500
123 bp) is detectable at nearly all chromosome ends [35,38] (**Fig. 1a, Supplementary Fig. 2**). Based on
124 these features, we classified chromosome ends into two categories: X-only ends, which contain
125 only the X element, and XY' ends, which include both X and Y' elements. Because X elements

126 are relatively small and therefore more difficult to annotate, we classified ends containing a Y′
127 element as XY′, whereas ends lacking a Y′ element were categorized as X-only. The two ends
128 without annotated X or Y′ elements (**Supplementary Fig. 2**) were included in the X-only category.

129 Meta-plots of Red1 and Hop1 profiles revealed that axis protein enrichment differed between
130 these two categories. X elements at X-only ends exhibited axis protein enrichment close to the
131 genome average, indicating that isolated X elements have a substantial propensity for axis protein
132 recruitment (**Fig. 1d**). By contrast, X elements at XY' ends showed Red1 and Hop1 enrichment
133 below the genome average (**Fig. 1d-e**). Meta-analyses revealed an axis protein binding site at
134 the telomere-proximal side of the Y' element that may act as a local sink for axis protein
135 recruitment (**Fig. 1f**).

136 The variable presence of Y' elements also raised the question of whether axis protein depletion
137 is more appropriately assessed by aligning chromosome ends at the X elements. However,
138 metagene analysis anchored on the X elements rather than the telomeres showed a substantially
139 weakened depletion signal in meta-analyses (**Supplementary Fig. 4a**). Although this weakened
140 signal is likely partly due to increased noise from incomplete X-element annotation, the more
141 uniform depletion when anchoring on telomeres indicates that the biologically relevant anchor for
142 the observed suppression of axis protein deposition is the chromosome end.

143 **Axis protein depletion near telomeres is encoded in *cis***

144 To determine whether the local suppression of axis protein binding is due to telomere proximity
145 or intrinsic sequence features, we analyzed chromosome fusions, in which subtelomeric domains
146 were relocated to the chromosome interior [39]. These chromosomes were constructed in two
147 different genetic backgrounds (S288c and SK1; **Fig. 2a**) and showed overall normal Red1
148 enrichment, except for regional changes around centromeres, as noted previously [39]. The need
149 for unique sequences during the fusion process invariably resulted in the deletion of some

150 subtelomeric sequences, but in two cases (S288c: chrI-L and SK1: chrIV-R) the fusion
151 breakpoints were only 6.8 and 11.3 kb from telomeres, allowing for analysis of effects on axis
152 protein enrichment in the subtelomeric domains. At those fused chromosome ends, axis protein
153 distribution mirrored that of native, unfused ends (**Fig. 2b**), suggesting that, at least at those ends,
154 reduced axis protein enrichment at chromosome ends is driven by specific sequences encoded
155 at chromosome ends rather than by telomere proximity.

156 To further test whether reduced axis protein enrichment is encoded in *cis*, we took advantage of
157 the strain-specific differences between the subtelomeres of S288c and SK1, by analyzing Red1
158 enrichment data from S288c/SK1 hybrids that harbor one haploid chromosome complement from
159 S288c and one complement from SK1 [39]. Because of the large number of sequence differences
160 between the two genomes, many reads can be uniquely assigned, enabling internally controlled
161 analysis of axis protein enrichment between the two genomes [36]. Comparison of individual
162 chromosome ends of S288c and SK1 showed that the presence of Y' elements and other
163 subtelomeric sequences primarily resulted in shifts of Red1 peaks toward the chromosome
164 interior (**Supplementary Fig. 5**). After correcting for this displacement, the relative distribution of
165 Red1 peaks and peak heights remained remarkably similar for matching ends (**Fig. 2c**). These
166 data indicate that changing the distance from the nearest telomere does not affect Red1 binding
167 patterns and imply that telomere-proximal axis protein enrichment is to a large extent hardwired
168 into the underlying DNA sequence. The fact that addition of a Y' element effectively places regions
169 of low Red1 binding further into the chromosome interior likely also explains why XY'-ends have
170 lower subtelomeric Red1 and Hop1 enrichment than X-only ends (**Supplementary Fig. 4b**).
171 Excluding all Y' element sequences from the averaging did not grossly alter this distribution,
172 indicating that the lower Red1/Hop1 enrichment at XY'-ends is not because of reduced axis
173 protein binding to Y' sequences.

174 Across the genome, gene-rich regions exhibit overall higher axis protein enrichment [13,16]. As the
175 subtelomeric domains are comparatively gene-poor [27,28], we asked how well local coding density
176 (the fraction of DNA that encodes open reading frames) correlated with axis protein enrichment.
177 This analysis revealed a strong correlation between the regions of reduced coding density and
178 Red1 depletion (**Fig. 2d**). In addition, binning the genome into 20-kb bins showed a positive
179 correlation between coding density and average Red1 binding, similar to the effect seen across
180 the genome (**Supplementary Fig. 4d**). Thus, reduced coding density may partially underlie the
181 reduced axis protein recruitment within 20 kb of telomeres, although we note that this correlation
182 was only apparent when Y' elements were excluded from the analysis. Interestingly, the
183 correlation was absent in the EARs (**Supplementary Fig. 4d**), presumably reflecting the
184 specialized regulation of axis protein deposition in these regions [19].

185 **Rec8-dependent and independent pathways mediate axis protein localization at**
186 **chromosome ends**

187 Chromosomal recruitment of Red1 and Hop1 is mediated by two parallel pathways. The meiotic
188 Rec8-cohesin complex preferentially recruits axis proteins to sites of convergent transcription [16],
189 whereas the chromatin-binding region (CBR) of Hop1 directs axis proteins to nucleosome-dense
190 regions ("islands") characterized by higher coding density [13,16]. We sought to determine whether
191 the depletion of axis proteins near chromosome ends could be attributed to reduced activity of
192 one of these pathways.

193 Intriguingly, Rec8-cohesin levels in the subtelomeric regions were comparable to the genome
194 average. Although enrichment trended slightly lower, the depletion was within the 95% confidence
195 interval of a bootstrapped distribution ($p = 0.37$) and thus was not significantly different from the
196 rest of the genome (**Fig. 1b-c**). Therefore, the depletion of Hop1 and Red1 in the subtelomeric
197 domains is not simply due to reduced Rec8-cohesin binding in these regions.

198 The regions enriched for Red1 and Hop1 in the telomere-associated sequences were also
199 enriched for Rec8: Rec8 was bound more strongly to the X elements of X-only ends than to XY'
200 ends (**Fig. 1d-e**) and formed a strong peak at the telomere-proximal side of Y' elements (**Fig. 1f**).
201 This peak coincided with the 3' end of the Y'-encoded open reading frame (ORF), consistent with
202 other chromosomal Rec8 peaks, which are typically enriched downstream of ORFs [16,40]. Previous
203 studies have demonstrated that active transcription can induce the sliding of the cohesin ring and
204 direct axis protein association to the end of ORFs [16,41,42]. Therefore, transcription of the Y' ORF
205 may similarly influence axis protein deposition within Y' elements.

206 The coincident binding of axis proteins and Rec8 supports the hypothesis that Rec8-cohesin is
207 an important contributor to axis protein deposition at chromosome ends. To directly test this
208 possibility, we examined Red1 binding in a *rec8* mutant strain using spike-in normalized ChIP-
209 seq datasets [13,36]. In the subtelomeric domains, Red1 levels were significantly reduced in the *rec8*
210 mutant compared to wild type (**Fig. 3a-b**). Importantly, the remaining Red1 enrichment was no
211 longer depleted in the subtelomeric domains. These data suggest that the molecular mechanism
212 that reduces axis proteins in the subtelomeric domains interferes with the Rec8-dependent
213 recruitment of axis proteins.

214 On the other hand, analysis of a *hop1-phd* mutant, which lacks the CBR [13,15], revealed only minor
215 effects in the subtelomeric domains (**Fig. 3a-b**). However, we consistently noted reduced Red1
216 binding in the neighboring EARs (**Fig. 3a**), implying a role for the Hop1 CBR in promoting axis
217 protein enrichment in the EARs. In line with the two recruitment mechanisms acting in parallel
218 [13,15], the persistent subtelomeric axis protein signal in *rec8* mutants was abolished upon
219 introduction of the *hop1-phd* mutation (**Fig. 3a-b**). Similar additive effects were observed in the X
220 and Y' sequences (**Fig. 3c-d**). These data indicate that both pathways of axis recruitment
221 contribute additively to Red1 binding at chromosome ends. However, the Rec8-dependent

222 pathway, which is responsible for recruiting the majority of Red1, is the regulatory target for the
223 relative depletion of axis proteins from chromosome ends.

224 **Dot1 is required for subtelomeric depletion of axis proteins**

225 Subtelomeric regions share qualitative similarities with pericentromeric regions, particularly in the
226 differential enrichment of axis proteins and Rec8-cohesin. Both regions show a relatively higher
227 abundance of Rec8-cohesin compared to Red1, with most data points falling below the genome-
228 wide regression line (**Fig. 4a**)**.** At pericentromeres, this differential enrichment of axis factors
229 persists even if the centromere itself is inactivated [39], indicating that the local DNA sequence or
230 chromatin environment influences axis protein binding. Given the distinct chromatin state of the
231 subtelomeric domains, we investigated whether chromatin modifiers specific to these regions
232 contribute to axis protein depletion.

233 We focused our analysis on histone marks related to meiotic DSB formation or those that are
234 specifically different in the subtelomeric domains [30,43-46]. ChIP-seq analysis identified two marks -
235 H3K4me3 and H3K79me3 - that closely matched the pattern of axis protein depletion (**Fig. 4b**).
236 Both marks are long-lasting indicators of active gene expression that are depleted from
237 subtelomeric domains [28,30] and have been implicated in the control of meiotic DSB formation [43,46].
238 We note that relative depletion is also apparent when comparing genes in the subtelomeric
239 domains to the rest of the genome by metagene analyses (**Supplementary Fig. 5a**), and thus is
240 not simply due to the lower coding density of the subtelomeric domains.

241 To explore the role of these histone modifications in axis protein depletion, we used spike-in
242 normalized ChIP-seq [36] to analyze Red1 in mutants lacking Set1 or Dot1, the enzymes
243 responsible for the trimethylation of H3K4 and H3K79, respectively. In *set1Δ* mutants,
244 subtelomeric Red1 binding patterns were indistinguishable from wild-type, although we observed
245 an overall reduction in Red1 binding (**Fig. 4c-e, Supplementary Fig. 6b-c**), consistent with

246 previous analyses [36]. In contrast, *dot1Δ* mutants exhibited a marked redistribution of Red1. Red1
247 levels were relatively elevated in the Y' and X elements and no longer significantly different from
248 genome average in the subtelomeric domains (p = 0.16) but were reduced in the EARs (**Fig. 4c-**
249 **e, Supplementary Fig. 6b-c**), indicating that Dot1 is an important regulator of axis protein
250 distribution. In addition, Red1 levels in *dot1Δ* mutants also trended lower in the pericentromeric
251 regions (p = 0.06 after Benjamini-Hochberg correction; **Supplementary Fig. 6d-e**). This effect is
252 opposite to the increase seen in the subtelomeric domains and indicates that subtelomeric
253 domains and pericentromeres use different mechanisms to achieve a relative depletion of Red1
254 compared to Rec8-cohesin.

255 To test whether the effects of Dot1 on Red1 recruitment are related to H3K79 trimethylation, we
256 analyzed mutants, in which H3 lysine 79 was changed to arginine (*hht1/2-K79R*) [46]. These
257 mutants recapitulated the drop in Red1 levels in the EARs (**Fig. 5a**), indicating that Dot1 promotes
258 axis protein binding in the EARs by methylating H3K79. However, Red1 levels in *hht1/2-K79R*
259 mutants also decreased in the subtelomeric domains and in the Y' and X elements (**Fig. 5a-d**)
260 and did not decrease in the pericentromeric regions (**Supplementary Fig 6d-e**). These
261 observations suggest that an H3K79-independent activity of Dot1 regulates axis protein
262 enrichment near chromosome ends and centromeres. MNase-seq analysis of *dot1Δ* mutants
263 failed to reveal obvious changes in chromatin accessibility in the subtelomeric domains or the
264 pericentromeres **(Supplementary Fig. 6f-g)**, suggesting that the effects on Red1 recruitment
265 seen in *dot1Δ* mutants are not the result of altered nucleosome occupancy.

266 As Dot1 primarily methylates H3K79 across gene bodies, we separated Red1 signals into genic
267 and intergenic regions. Intriguingly, the reduced binding of Red1 in the chromosome interior in
268 *dot1Δ* mutants primarily affected intergenic regions whereas the increase in Red1 association
269 near chromosome ends in *dot1Δ* mutants occurred predominantly on gene bodies (**Fig. 4f**). These
270 data indicate that the chromatin requirements for axis protein recruitment differ between

271 chromosome ends and the chromosome interior and that Dot1 plays multiple roles in controlling
272 axis protein recruitment, only some of which require H3K79 methylation.

273 **Effects of Dot1 on axis protein deposition depend on Sir3**

274 The Sir complex is an important regulator of telomere-associated chromatin. Indeed, one
275 consequence of losing Dot1-mediated H3K79 methylation is a deregulation of the Sir complex
276 [47,48]. To test whether the Sir complex has a role in telomere-proximal axis protein deposition, we
277 determined the distribution of Red1 in *sir3* mutants using spike-in normalized ChIP-seq analysis.
278 Binding levels of Red1 in the EARs were higher in *sir3* mutants (**Fig. 6a**), consistent with previous
279 analyses of Hop1 in *sir2* mutants [19], but meta-analysis revealed no significant difference in the
280 average depletion of Red1 in the last 20 kb between *sir3* and wild-type strains (**Fig. 6a-b**).
281 Similarly, meta-plots of average Red1 profiles on X and Y' elements in *sir3* mutants showed no
282 new peaks compared to wild-type (**Fig. 6c-d**), although enrichment levels were lower on both
283 types of X element (**Fig. 6c**). Thus, the Sir complex is not a major regulator of telomere-proximal
284 axis protein depletion in the presence of *DOT1*.

285 Intriguingly, however, mutation of *sir3* reversed many of the Red1 recruitment phenotypes of
286 *dot1Δ* mutants, including the increased Red1 binding in the subtelomeric domains and the
287 decreased binding in the EARs and pericentromeres (**Fig. 6a-b, Supplementary Fig. 7a-b**).
288 Moreover, the binding pattern of Red1 across X and Y' elements in the *sir3 dot1Δ* double mutant
289 matched the phenotype of the *sir3* mutant rather than the *dot1Δ* mutant (**Fig. 6a-b**). This
290 phenotypic epistasis suggests that Dot1 either counteracts the activity of the Sir complex to
291 control Red1 distribution or else that absence of *DOT1* creates an environment in which the Sir
292 complex can influence axis protein recruitment.

293 **Conservation of Sir-dependent telomeric heterochromatin during meiotic recombination**

294 To better understand the role of the Sir complex in meiosis, we analyzed the genomic distribution
295 of Sir3 in wild-type cells by ChIP-seq. In vegetative cells, the Sir complex establishes silent
296 chromatin domains at mating-type loci and telomere-associated sequences [49,50]. At some
297 chromosome ends, Sir chromatin also spreads from the X element into the neighboring
298 subtelomeric domains [29,51], although spreading across entire subtelomeric domains is only
299 observed under conditions of Sir overexpression [30].

300 Our analyses at the time of meiotic induction and during the peak of DSB formation (3 hours post-
301 induction) revealed consistent Sir3 binding patterns (**Fig. 7a, Supplementary Fig. 8**). In addition
302 to the telomere-proximal silent mating type loci on chrIII (*HML*, *HMR*), Sir3 was enriched at both
303 types of X elements, although binding on X elements at XY' ends was lower than that observed
304 at X-only ends (**Fig. 7a-b**). Sir3 was also enriched upstream of the 5' end of the Y'-encoded ORF
305 (**Fig. 7c**). In addition, we observed limited and heterogeneous spreading of Sir3 from subtelomeric
306 X elements into adjacent domains on certain chromosome ends. For example, on chrVII-L, Sir3
307 spread approximately 6 kb from the X element during early prophase I (3 hours post-induction),
308 whereas no detectable spreading occurred on chrVI-L (**Fig. 7d-e**). Spreading distances varied
309 across chromosome ends (**Supplementary Fig. 9a-b**) and did not correlate with the presence of
310 Y' elements (**Supplementary Fig. 8**), mirroring the behavior of Sir proteins in vegetative cells
311 [29,30]. These findings indicate that Sir-dependent telomeric heterochromatin remains largely
312 unchanged as cells initiate meiotic recombination.

313 To determine whether subtelomeric domains with Sir3 spreading exhibit altered transcription of
314 underlying genes, we conducted mRNA-seq analysis on samples collected 3 hours post-meiotic
315 induction in the presence or absence of *SIR3*. Plotting relative fold changes in mRNA levels as a
316 function of the average Sir3 occupancy in the 250 bp upstream of each ORF revealed a significant
317 correlation between Sir3 occupancy and increased mRNA levels upon *SIR3* deletion (**Fig. 7f**).
318 Given the prominent Sir3 peak observed at the start of the Y' element metaplot (**Fig. 7c**), we also

319 analyzed Y' element expression 3 hours after meiotic induction. The average Y' element
320 expression was significantly increased in the absence of *SIR3* (**Supplementary Fig. 9c**). These
321 results indicate that the transcriptional effects of Sir3 are linked to sequences where Sir3 binds,
322 as detected by ChIP-seq.

323 Sir-dependent transcriptional silencing in vegetative cells is thought to occur by chromatin
324 compaction and promoter occlusion [52]. MNase-seq analysis of wild type and *sir3* mutants 3h after
325 meiotic induction, revealed a strong Sir3-dependent drop in the relative number of sequenced
326 MNase cleavage fragments in the subtelomeric domains, consistent with chromatin compaction
327 (**Fig. 7g**). Interestingly, the effects on chromatin compaction as measured by MNase-seq
328 extended across more than 20 kb, contrasting with the much more limited extent of detectable
329 Sir3 spreading (**Supplementary Fig. 9a**). These data indicate that Sir3 can influence chromatin
330 compaction even in regions where it is not measurably enriched, possibly through the role of the
331 Sir complex in anchoring telomeres to the nuclear envelope [53].

332 **Sir proteins protect X elements and regions of Sir spreading from meiotic DSBs**

333 We wondered how Sir-dependent heterochromatin (mediated by the Sir2-Sir3-Sir4 complex) and
334 Dot1-dependent axis protein suppression interface with the meiotic DSB machinery near
335 chromosome ends. Genome-wide DSB levels had previously been determined by microarray
336 analysis in *sir2Δ rad50S* strains, but the repetitive nature of the subtelomeric domains had limited
337 coverage, and the X and Y' elements were not included [54]. More recently, DSB formation in *sir2Δ*
338 strains was also analyzed using Spo11-oligo sequencing [19], which sequences the DNA fragments
339 that remain covalently attached to Spo11 after cleavage [11], although telomere-proximal DSB
340 formation was not investigated in that study. Analysis of the Spo11-oligo dataset revealed a
341 significant increase in DSB levels on X elements but not Y' elements in *sir2Δ* strains (**Fig. 8a**).
342 This pattern mirrors the relative enrichment of Sir3 in these elements, indicating that Sir chromatin

343 suppresses DSB formation in the X elements. In addition, DSB formation was somewhat
344 increased in the subtelomeric domains in *sir2Δ* mutants. Increased DSB induction was correlated
345 with the extent of Sir3 occupancy in wild-type cells (**Supplementary Fig. 10a**). Accordingly,
346 increased DSB formation was also correlated with elevated gene expression in the same regions
347 in *sir3* mutants but not in the rest of the genome (**Supplementary Fig. 10b**). These findings
348 suggest that elevated promoter openness, which enables increased gene expression, also
349 creates a window for meiotic DSB formation.

350 To complement and expand this analysis, we analyzed *sir3, dot1Δ*, and *sir3 dot1Δ* mutants by
351 TrAEL-seq, which sequences the exposed 3' ends that result from Spo11 cleavage [55]. To avoid
352 signal changes due to DSB repair, this analysis was conducted in a repair-defective *dmc1Δ*
353 background [56]. We observed several distinct effects on DSB formation near chromosome ends.
354 Consistent with the Spo11–oligo measurements in *sir2Δ* mutants, average hotspot intensity was
355 significantly increased within 5 kb of X elements and the number of significant DSB hotspots
356 nearly doubled in the same regions in strains lacking *SIR3* (**Fig. 8b-c**). Increased DSB formation
357 occurred specifically at sites of increased MNase accessibility (**Fig. 8d**), supporting the model
358 that Sir-dependent DNA occlusion suppresses DSB formation in the heterochromatic parts of the
359 subtelomeric domains. On the other hand, deletion of *DOT1* did not measurably alter DSB
360 formation in the 20 kb from chromosome ends (**Fig. 8b-d**), showing that the increased axis protein
361 deposition in these regions does not translate into higher DSB activity. We also note that overall
362 hotspot activity in the subtelomeric domains remained substantially below genome average in all
363 mutants (**Fig. 8d-e**), indicating that additional layers of regulation contribute to DSB suppression
364 at chromosome ends.

365 Intriguingly, TrAEL-seq analysis indicated differing genetic interactions between *DOT1* and *SIR3*
366 in other parts of the genome. The most notable large-scale effect was a decrease in DSB levels
367 in the *sir3 dot1Δ* double mutants 30-100 kb from chromosome ends, a genomic range that largely

368 overlaps with the EARs (**Fig 8e**). The reason for this reduction is unclear but may reflect
369 premature downregulation of DSBs in the EARs, which normally experience a longer window of
370 DSB formation [19]. Further highlighting the different genetic interactions between *DOT1* and *SIR3*,
371 DSB formation around centromeres was decreased to a similar extent in *dot1Δ* and *sir3* single
372 mutants (**Supplementary Fig. 11a**), whereas DSB levels were increased around the ribosomal
373 DNA locus in a Sir3-dependent manner in *dot1Δ* mutants (**Supplementary Fig. 11b**), consistent
374 with previously observed Sir-dependent DSB induction in this region [57]. As discussed below, the
375 different interactions suggest a combinatorial code that allows these two chromatin regulators to
376 adjust meiotic recombination in a region-specific manner.

377 **Discussion:**

378 Here, we show that key effectors of meiotic recombination, namely axis proteins and the DSB
379 machinery, are suppressed by multiple layers of regulation at chromosome ends. We identified
380 two chromatin regulators, Dot1 and the Sir complex, which contribute to locally suppressing axis
381 protein deposition and DSB formation, respectively. However, additional layers of regulation
382 clearly exist, as DSB levels remain substantially below genome average in *dot1 sir3* double
383 mutants. Additional regulatory layers likely also explain why increases in axis protein binding as
384 observed in *dot1* mutants are not sufficient to increase DSB formation in these regions.

385 Our data suggest that downregulation of axis protein binding near chromosome ends does not
386 require telomere proximity because placing subtelomeric domains into the chromosome interior
387 of fusion chromosomes did not detectably alter axis protein enrichment. Accordingly, axis protein
388 binding patterns was also remarkably consistent between two different strain backgrounds despite
389 altered distances from the telomeres. These data indicate that the signals that govern the local
390 reduction in axis protein binding are at least partly encoded in *cis.* The molecular nature of these
391 suppressive signals remains to be delineated but our data revealed an intriguing correlation with

392 the reduced coding density of the subtelomeric domains, which tracks remarkably well with the
393 depletion of axis proteins. However, other *cis*-regulatory aspects such as differential replication
394 timing [33,58] may also be responsible for the overall lower axis protein levels.

395 In addition, Dot1 negatively regulates axis protein deposition in X and Y' elements and the
396 subtelomeric domains. This activity does not require H3K79 trimethylation and thus either
397 depends on other methylation targets or on Dot1's methyltransferase-independent activities,
398 several of which have been described [59,60]. Dot1 presumably interferes with Rec8-dependent axis
399 protein recruitment as our analyses suggest that this pathway is specifically weakened near
400 chromosome ends (**Fig. 9**). Given that Rec8 is not significantly depleted near chromosome ends,
401 this interference must specifically impact the interaction between Rec8 and Red1 [16].

402 Intriguingly, the increased axis protein deposition in *dot1Δ* mutants is rescued by deletion of *SIR3*.
403 This phenotypic epistasis suggests that Dot1 may counteract the activity of Sir3 to regulate
404 telomere-proximal axis protein deposition. Alternatively, the absence of *DOT1* may create a
405 chromatin environment that allows Sir3 (and by extension the Sir complex) to regulate axis protein
406 binding. This second possibility is supported by the observation that loss of Sir3 (or Sir2 [19]) alone
407 does not detectably affect the suppression of axis proteins in the subtelomeric domains. An
408 interplay between the Sir complex and Dot1 was previously shown to affect checkpoint regulation
409 during meiotic recombination, although we note that in that situation, loss of *sir2* and *dot1* both
410 inactivate checkpoint activity possibly because of a redistribution of Sir2 away from sites of
411 checkpoint activity in *dot1* mutants [61]. In vegetative cells, Dot1 helps constrain Sir-protein
412 dependent silencing both through H3K79 trimethylation and by competing for the same
413 nucleosomal binding site [62]. This two-pronged mechanism may explain why mutation of H3K79
414 was not sufficient to recapitulate the increased axis protein deposition seen in *dot1Δ* mutants.
415 Interestingly, even though the axis proteins act as recruitment platforms for the DSB machinery
416 [12], increased axis protein deposition was not sufficient to increase DSB formation in the telomere-

417 proximal sequences in *dot1Δ* mutants, indicating that additional layers of regulation suppress DSB
418 formation in these regions.

419 In addition to its role in regulating axis proteins, we show that the Sir complex suppresses DSB
420 formation at a small number of subtelomeric hotspots through local chromatin compaction of gene
421 promoters, the preferred DNA substrates for DSB formation in yeast [11]. Our data strongly imply
422 that DSB suppression is a direct consequence of the enrichment of Sir3 in these regions.
423 Furthermore, the strict spatial overlap between increased MNase sensitivity and sites of DSB
424 formation in *sir3* mutants supports the notion that nucleosomes interfere with meiotic DSB
425 formation, presumably by restricting access to the DNA substrate [11,45 63]. However, our data also
426 show that the increased MNase sensitivity in *sir3* mutants extends across more than 20 kb from
427 telomeres, whereas hotspot activation is much more spatially restricted. These data indicate that
428 increased DNA accessibility alone is in most cases not sufficient to activate meiotic DSB formation
429 in the subtelomeric domains.

430 While this study focused on the subtelomeric regions, our genome-wide data also showed effects
431 of Dot1 and the Sir complex in other parts of the genome, including the EARs, the
432 pericentromeres, and the rDNA-flanking regions. H3K79me3 is abundantly present in those
433 regions, and Dot1's distribution in vegetative cells closely matches H3K79me3 [64], suggesting that
434 Dot1 and H3K79me3 may directly influence axis protein deposition and/or DSB formation in those
435 regions. By contrast, Sir3 is not noticeably enriched in the EARs or the pericentromeres in our
436 analyses, although genome-wide effects of *sir* mutation on meiotic DSB formation were also noted
437 previously [54]. It is possible that the Sir complex levels in these regions are too low to measure
438 confidently. Alternatively, some effects may be indirect as both the Sir complex and Dot1 are
439 transcriptional regulators and thus could change the expression levels of key meiotic regulators
440 to modulate regional axis protein deposition or DSB activity. Such indirect effects may also

441 contribute to the varying genetic interactions between the Sir complex and Dot1 observed in
442 different genomic regions.

443 Chromosome ends differ in their sequence composition, spreading of the Sir complex, and the
444 location of genes, DSB hotspots, and axis binding sites, creating inherently chromosome end-
445 specific variability in the range and presence of individual suppressive effects. Nevertheless,
446 downregulation of axis protein deposition and DSB induction within about 20 kb from chromosome
447 ends is remarkably uniform (**Supplementary Fig. 3a-b**). Thus, an overall selective pressure likely
448 exists to reduce axis protein binding and DSB induction at chromosome ends, and multiple
449 molecular mechanisms have the potential to satisfy this goal.

450 One selective pressure near chromosome ends is the need to suppress meiotic crossovers.
451 Telomere-proximal crossovers are less effective at maintaining linkages between homologous
452 chromosomes [65] and are associated with increased risk of Down syndrome in humans [23,24]. Axis
453 proteins, in particular, are a logical target for such suppression, as they not only recruit DSB
454 factors but also help target DSB repair to homologous chromosomes by preventing sister
455 chromatid recombination [66]. Favoring repair from sister chromatids may also reduce the risk of
456 non-allelic recombination events. Chromosome ends are especially prone to non-allelic
457 homologous recombination because of their repetitive sequences and the close physical proximity
458 of telomeres along the nuclear envelope during meiotic prophase [21,67,68]. Having multiple
459 regulatory layers independently suppress axis protein deposition and DSB formation may thus
460 establish a robust protective mechanism to shield chromosome ends from non-allelic and
461 unproductive recombination and ensure proper meiotic chromosome segregation.

462

463 **Methods and Materials:**

464 **Yeast strains and growth conditions:**

465 All the strains utilized in this study belonged to the SK1 background, except for the analysis using
466 the published fusion chromosome strains, which were SK1/S288C hybrids, and the spike-in
467 analysis, which used meiosis-competent S288c (SK288c) strains (see Methods: Spike-in
468 Normalization). The genotypes are detailed in **Supplementary Table 1.** For experiments using
469 vegetative cells, cultures were grown in YPD medium overnight at room temperature until
470 saturation. The following day, the cells were diluted to an OD_{600} of 0.2 and incubated at 30°C until
471 they reached an OD_{600} of 1. At this stage, 50 ml of culture was collected for ChIP-seq.

472 To induce synchronous meiotic cultures, strains were grown for 24 hours in YPD medium at room
473 temperature. Cells were enriched in the G1 phase by inoculating them at OD_{600} = 0.3 in pre-
474 sporulation BYTA medium (1% yeast extract, 2% bactotryptone, 1% potassium acetate, 50 mM
475 potassium phthalate) for 16.5 hours at 30°C. Cells were washed twice with sterile water and
476 transferred into SPO medium at OD_{600} = 1.9 (SPO: 0.3% potassium acetate, 0.001% acetic acid).
477 Cultures were incubated at 30°C on a shaker, and the time of inoculation into SPO was defined
478 as T = 0 hours. At the specified timepoints, 25 ml of culture was collected for ChIP-seq and 1.6
479 ml for mRNA-seq. The synchrony of meiotic cultures was validated using flow cytometry.

480 **Chromatin immunoprecipitation (ChIP) & Illumina sequencing:**

481 Cells collected at the indicated timepoints (T = 3h unless noted otherwise) were pelleted and
482 immediately crosslinked for 30 minutes in a 1% formaldehyde solution at room temperature with
483 gentle shaking. Subsequently, the crosslinking reaction was quenched by incubating the cells for
484 5 minutes at room temperature in a 125 mM glycine solution. Following this, the cells were
485 processed according to the protocol outlined in [16] and immunoprecipitated with 2.5 µl of either
486 anti-Sir3 (HM01065, kind gift of Stephen Bell, MIT), anti-Red1 (#16440, kind gift of N.
487 Hollingsworth) or anti-H3K79me3 (abcam, ab2621). For spike-in normalization (SNP-ChIP [36]),

488 SK288c cross-linked meiotic samples were added to respective samples at 20% prior to ChIP
489 processing. Library preparation, quality, and quantity checks were then performed as described
490 in [15]. All the prepared chromatin immunoprecipitation (ChIP & SNP-ChIP) libraries were
491 sequenced as 150-bp paired-end reads on Illumina NextSeq 500 or Element Biosciences' Aviti
492 instruments. The sequencing runs were conducted by the Genomics Core at New York University
493 Center for Genomics and Systems Biology.

494 **Processing ChIP-seq reads from Illumina sequencing:**

495 Illumina sequencing reads were aligned to the SK1 genome [35] using Bowtie 2 (Version 2.4.2) [69].
496 To improve mapping of reads to repetitive subtelomeric regions, the Bowtie 2 read reporting mode
497 was configured to allow multiple alignments, reporting the best match. MACS2 2.1.1 was used to
498 extend reads in the 5'-> 3' direction to a final length of 200 nt. SPMR (signal per million reads)
499 normalization was applied to both input and ChIP pileups using MACS2. The resulting fold-
500 enrichment files were used for downstream analysis in R. The ChIP-seq pipeline and analysis
501 scripts are available on the Hochwagen Lab GitHub page
502 https://github.com/hochwagenlab/ChromosomeEnds.git.

503 **mRNA-sequencing & analysis:**

504 mRNA was extracted from cells collected at T = 3h. mRNA extraction, first- and second-strand
505 synthesis, and library preparation were conducted following the procedures outlined in [70]. The
506 resulting libraries were sequenced as 150-bp paired-end reads on an Illumina NextSeq 500
507 instrument. The sequencing run was executed by the Genomics Core at New York University
508 Center for Genomics and Systems Biology. The GTF (General Transfer Format) file was modified
509 to include all completely annotated Y' elements. Subsequently, reads obtained from Illumina
510 sequencing were aligned to the SK1 genome [35], and the counts mapping to the modified SK1 gtf

511 file were determined using the nf-core RNA-Seq pipeline [71]. The relative abundances, measured
512 as transcripts per million (TPM) in Salmon [72], were used for downstream analysis in R.

513 **Spo11-oligos mapping:**

514 Published Spo11-oligo datasets from WT and *sir2Δ* strains [19,73] were analyzed. Adaptors were
515 removed from the reads using fastx_clipper from the FASTX Toolkit (version 0.0.14) and reads
516 shorter than 15 nt were discarded. The clipped reads were aligned to the SK1 genome [35] using
517 Bowtie 2 (Version 2.4.2) [69]. The read alignment mode was set to local, and the reporting mode
518 allowed multiple read alignments while reporting the best alignment. SPMR (signal per million
519 reads) normalization was performed on the read pileups.

520 **Mononucleosomal DNA preparation:**

521 For MNase-seq, 50 ml of synchronized meiotic cultures was harvested at T = 3h and crosslinked
522 with 1% formaldehyde for 30 minutes at room temperature. Crosslinking was quenched with
523 125 mM glycine, and cells were spheroplasted in Buffer Z (0.5 M sorbitol, 50 mM Tris-HCl pH 7.4,
524 10 mM β-mercaptoethanol) containing zymolyase T100. Spheroplasts were pelleted and
525 resuspended in NP buffer (1 M sorbitol, 50 mM NaCl, 10 mM Tris-HCl pH 7.4, 5 mM $MgCl_2$, 1 mM
526 $CaCl_2$, 0.5 mM spermidine, 1 mM β-mercaptoethanol, 0.075% NP-40) and digested with 5–80
527 units of micrococcal nuclease (MNase; Thermo Fisher Scientific, EN0181). MNase was diluted
528 from a 300 U/µl stock to 20 U/µl, and mononucleosome-sized fragments were consistently
529 obtained using 2 µl of a 1:4 dilution of the 20 U/ µl stock (final concentration 5U/µl; 10 units in
530 total). Digestions were stopped with SDS and EDTA, followed by proteinase K treatment and
531 overnight incubation at 65°C. Subsequent steps, including DNA purification and library
532 preparation, were performed as described in [11]. Libraries were sequenced as 150-bp paired-end
533 reads on an Illumina NextSeq 500, and the sequencing run was carried out by the Genomics Core
534 at the New York University Center for Genomics and Systems Biology.

535 **MNase-seq data analysis:**

536 To improve read alignment in repetitive subtelomeric regions, Bowtie 2 was configured to report
537 multiple alignments using the "best match" mode as described for ChIP-seq. For signal
538 quantification, fragments were processed with MACS2 (--nomodel --keep-dup all --SPMR) to
539 generate normalized coverage tracks. To map MNase cleavage sites at nucleotide resolution, the
540 5' end of each properly paired fragment was extracted from BAM files. This yielded single-base
541 BED files representing MNase cut frequency, which were used for downstream metaplot analysis
542 of chromatin accessibility.

543 **Plug preparation for TrAEL-seq:**

544 Plugs were prepared from meiotic cultures harvested at T = 5h to allow for accumulation of DSBs
545 in the *dmc1* mutant background. For each strain, 20 ml of culture was pelleted and washed twice
546 with CHEF TE buffer (10 mM Tris-HCl, pH 7.5, 50 mM EDTA, pH 8.0). The cell pellet was
547 resuspended in 300 µl CHEF TE, followed by the addition of 4 µl zymolyase T100 (10 mg/ml).
548 The mixture was briefly vortexed and incubated at 42°C for approximately 30 seconds. Low-
549 melting-point agarose (1% SeaPlaque GTG in 125 mM EDTA, pH 8.0), prewarmed to 42°C, was
550 added and transferred into plug molds. Plugs were solidified on ice for 10 minutes before being
551 transferred into LET buffer (10 mM Tris-HCl, pH 7.5; 0.5 M EDTA, pH 8.0). Plugs were incubated
552 overnight at 37°C. The following day, plugs were treated with proteinase K in NDS buffer (10 mM
553 Tris-HCl, pH 7.5; 0.5 M EDTA; 1% N-lauroylsarcosine) at 50°C overnight. After digestion, plugs
554 were washed sequentially: first with CHEF TE for 1 hour at room temperature, followed by two
555 washes with ice-cold CHEF TE containing 10 µl freshly prepared PMSF (100 mM) in ethanol, with
556 each wash incubated for 1 hour in the cold room. A fourth wash was performed with RNase T1 in
557 CHEF TE, incubated at 37°C for 1 hour, followed by a final wash with CHEF TE at room
558 temperature for 1 hour. Plugs were stored at 4°C in CHEF TE until further use.

559 **TrAEL-seq Library Preparation, Sequencing, and Data Analysis:**

560 TrAEL-seq library preparation, sequencing and data analysis were conducted following the
561 procedures outlined in [55]. TrAEL-seq signal pileups were generated using MACS2 (v2.2) and
562 normalized pileups were generated using SPMR normalization. Downstream analyses were done
563 in R. We note that telomeres can have free 3' ends that lead to a Spo11-independent TrAEL-seq
564 signal. Because this signal showed strong batch effects that impacted the nearby Y' and X
565 elements, we were unable to confidently analyze DSB formation in Y' and X elements using this
566 method.

567 **Statistical data analysis:**

568 1) **Spike-in normalization:** To allow for quantitative comparisons of chromatin
569 immunoprecipitation (ChIP) enrichment between different strains or conditions, we
570 performed spike-in normalization using SNP-ChIP [36]. A known amount of SK288c
571 chromatin (S288c strains engineered to efficiently enter meiosis) was used as a spike-in
572 control, with sequence reads mapping to the S288c genome serving as a reference for
573 normalizing sequencing depth and ChIP efficiency. The ratio of SK1 reads to S288c reads
574 was then used to scale the enrichment values, allowing for direct comparison of protein
575 abundance across different samples. This method is particularly useful for quantifying
576 relative changes in protein occupancy between mutant and wild-type strains. Data sets
577 from single strains, such as the analysis of wild-type strains presented in **Fig. 1**, were
578 analyzed without spike-in normalization, as no common denominator was necessary for
579 these analyses.
580 2) **Distance from telomeres plots:** The x-axis represents the distance from the annotated
581 telomeric repeats, beginning at telomeres and extending inward. The y-axis indicates
582 signal intensity, normalized so that the genome-wide average equals 1, or spike-in

583 normalized values where applicable. Data were processed as in [19] by binning signals into
584 consecutive 200-bp windows, followed by kernel smoothing to minimize noise and
585 highlight underlying trends.

586 3) **Bootstrapping plots:** Violin plots represent bootstrapped distributions obtained by
587 performing 1000 iterations of resampling, where, for each iteration, 32 regions of 20 kb (or
588 16 regions for centromeric analyses) were sampled with replacement. The violin plots
589 display the resulting distributions, indicating the median values along with two-sided 95%
590 confidence intervals. Two-sided empirical p-values were computed against this
591 distribution and BH-corrected. Effect sizes were measured via Cohen's d,

592 $$d = (\text{observed} - \mu_\text{boot})/\sigma_\text{boot}$$

593 where observed is the mean fold-enrichment in the focal regions; μ_boot is the mean of
594 the bootstrap distribution of means; and σ_boot is the standard deviation of that bootstrap
595 distribution.

596 4) **Metagene analyses, and meta-X and Y' elements plots:** Only fully annotated X/Y'
597 elements were analyzed; partially annotated copies were excluded because boundary-
598 anchored profiles required accurate start and end coordinates. The excluded partial X
599 elements are indicated with stars in **Supplementary Fig. 2** (coordinates: VIII:9643-9820,
600 X:15487-15645, XII:1020084-1020314, XV:1047720-1047878, XVI:9407-9565).
601 Metagene analyses followed previously published approaches [13]. Similarly, to align
602 variable-length X and Y' elements, we proportionally extended flanking regions based on
603 the element length (100% extension for X elements and 50% for Y' elements, as indicated
604 in the figure legends). Each extended region was then divided into 100 equal bins, scaling
605 each element to fixed relative positions: X elements occupied the middle third (bins 33–
606 66), and Y' elements occupied the middle half (bins 25–75). Signal intensities were
607 averaged across these bins, ensuring proportional alignment at element boundaries (e.g.,

608 bin 33 corresponded to the start of X elements, bin 25 corresponded to the start of Y'
609 elements).

610 5) **Confidence bands vs. bootstrapping:** We used different approaches to determine
611 significance depending on the structure of the underlying data. For metaplots of gene
612 bodies, X, or Y' elements, the structure of the underlying sequences, and hence the
613 distribution of chromatin marks and axis proteins, was relatively consistent after adjusting
614 for the length of the elements. This structure allowed meaningful confidence bands to be
615 shown. By contrast, the distribution of axis binding sites was inherently sparse and differed
616 between chromosome ends. As a result, a confidence band was not meaningful as the
617 differences in the positions of axis sites would drown out consistent differences in signal
618 across ends. To circumvent this problem, we instead combined the signal of the entire
619 region and evaluated how significantly different the mean was from the rest of the
620 chromosome using bootstrapping.

621 6) **Quantification of Red1 and Rec8 signals:** Rec8 peaks in **Fig. 4a** were derived from
622 Rec8 ChIP-seq data in wild-type cells (the same dataset used in **Fig. 1b-f**). For each Rec8
623 peak region, the Red1 signal was calculated as the average score across the entire Rec8
624 peak interval. Peaks were annotated as centromere-proximal (within ±10 kb of a
625 centromere), telomere-proximal (within 20 kb of a chromosome end), or non-
626 centromere/non-telomere to contextualize their genomic distribution. If peak regions were
627 straddling the boundaries, they were included as centromere-proximal/telomere-proximal.
628 Straddling Peaks: Centromeres 0.16% and telomeres 0.08% of total peaks. We used Rec8
629 peaks because the Rec8 signal did not change significantly compared to genome average
630 in the subtelomeric regions. The reduction of Red1 signal near telomeres meant that some
631 sites that have abundant Rec8 binding near telomeres did not have sufficient Red1 binding
632 to be called as peaks.

633 7) **Quantification of Sir3 spreading from chromosome ends:** Sir3 spreading was
634 quantified using a custom R pipeline. For each condition, ChIP-seq fold-enrichment over
635 input (FE) signals were extracted from chromosome-end regions from the X element
636 toward the centromere. These regions were divided into consecutive 250 bp bins, and the
637 average FE score was calculated for each bin. A dynamic threshold was defined as the
638 upper bound of the 95% confidence interval of genome-wide FE values. Spreading was
639 identified starting at the X-element boundary as the first continuous stretch of bins with FE
640 scores above this threshold. The spreading region was considered to end when two
641 consecutive bins fell below the threshold; the final bin above threshold before this drop
642 marked the endpoint of Sir3 spreading. Spreading distances were aggregated across
643 chromosome ends and visualized using violin plots.
644 8) **Promoter correlation plots:** Promoters were defined as the 250-bp window immediately
645 upstream of annotated genes. Spo11-oligo signal was HPM-normalized and averaged per
646 promoter in WT and *sir2Δ*. We plotted $\log_{10}$(*sir2Δ*/WT). To avoid inflated ratios from near-
647 zero denominators, we set a data-driven floor at the 2nd percentile of promoter means
648 pooled across WT and *sir2Δ* and excluded promoters only when both WT and *sir2Δ* means
649 were below this floor (117 out of 5541; 2.11%). Results were robust to using a 5% floor
650 (correlations changed only minimally). After filtering, the plotted set contained 34 genes
651 within 5 kb of an X element (blue) and 5,356 other genes (red). The same promoter set
652 was used for **Fig. 7f** and **Supplementary Fig. 10a–b**. RNA-seq fold changes were
653 obtained with DESeq2 (two biological replicates per condition) and are shown as $\log_{10}$.
654 Sir3 ChIP was genome-normalized (ChIP/Input). Values are means of two independent
655 biological replicates and were reproducible between replicates.
656 9) **Hotspot calling in TrAEL-seq data:** DSB hotspots were identified from TrAEL-seq data
657 using MACS2 (narrowPeak mode) on pooled biological replicates for each genotype, with
658 the q-value (FDR) threshold set to control the false discovery rate. Hotspot totals were:

659 *dmc1Δ* (n = 3,242), *sir3 dmc1Δ* (n = 3,224), *dot1Δ dmc1Δ* (n = 3,182), and *sir3 dot1Δ*
660 *dmc1Δ* (n = 3,130). For quantification, signal was taken from MACS2 treat_pileup
661 bedGraphs (RPM) and summarized as the mean RPM across each hotspot interval. For
662 each telomere, the 0–20 kb region inward of the annotated X-element was tiled into 5-kb
663 bins (bins 1–4 from the X element). Each hotspot was assigned to exactly one bin using
664 its start coordinate, preventing double-counting of hotspots that span multiple bins.

665 **Supporting information:** Supplementary Figures and Tables are attached in a word document.

666 **Data reporting:** The datasets generated and analyzed in this paper, excluding published
667 datasets, have been deposited in the Gene Expression Omnibus (GEO). The datasets can be
668 accessed with the accession numbers GSE287129 (ChIP-seq), GSE287127 (mRNA-seq), and
669 GSE287130 (TrAEL-seq). Additionally, all ChIP-seq datasets used in this study are listed in
670 **Supplementary Table 3**, and all Spo11-oligo, mRNA-seq, and TrAEL-seq datasets are listed in
671 **Supplementary Table 4**.

672 **Conflict of interest:** The authors declare no conflicting interests.

673 **Acknowledgements:**

674 We thank Stephen P. Bell for generously providing the Sir3 antibody, N. Hollingsworth for the
675 Red1 antibody, and A. Shinohara for the *hht1/2-K79R* strains. We also acknowledge the
676 Genomics Core at the New York University Center for Genomics and Systems Biology for their
677 valuable technical assistance and expertise in data processing. This work was supported in part
678 by the NYU IT High-Performance Computing resources, services, and staff expertise. We are
679 grateful to the Zegar Family Foundation for their generous support. TrAEL-seq library sequencing
680 and processing were performed by the Genomics (Geno06) and Bioinformatics (Bioinf01) teams
681 at the Babraham Institute, which receive financial support from the Institute Core Capability Grant

682 (BBSRC CCG). This research was financially supported as part of NIH grant R35 GM148223 to
683 A.H. A.R.R. acknowledges support from a Fleur Strand Graduate Fellowship from the Department
684 of Biology, as well as a Henry MacCracken Fellowship and a Dean's Dissertation Fellowship from
685 the NYU Graduate School of Arts and Science. J.H. acknowledges funding from the BBSRC (BI
686 Epigenetics ISP; BBS/E/B/000C0523), and K.M. acknowledges funding from the BBSRC
687 (BB/W509917/1). The funders had no role in the preparation of this manuscript.

688 **Author contributions:** Conceptualization - A.R.R., V.V.S., H.G.B., and A.H; Investigation &
689 Formal analysis - A.R.R., K.M., V.V.S., H.G.B., N.J.P., J.H., A.H; Computational Pipeline
690 development - A.R.R.; Manuscript writing (initial draft) - A.R.R. and A.H.; Manuscript editing - all
691 authors.

692 **Figures:**
693
694
695 **Figure 1: Distinct axis-protein enrichment patterns at chromosome ends.**
696 **(a)** Schematic of chromosome-end architecture in *S. cerevisiae*. XY′ ends contain Y′ elements; X-
697 only ends lack Y′ elements. We define the subtelomeric domains as encompassing the last 20 kb
698 from chromosome ends; they thus also encompass any X or Y' elements. The adjacent EARs
699 extend 20-120kb from ends. **(b)** Mean enrichment of Rec8 (light blue), Red1 (red), and Hop1
700 (purple) versus distance from telomeres in wild type (WT) early prophase I (T = 3h) from published
701 data [16,19,36], normalized to a genome average of 1 (gray dashed line; see Methods: Distance from
702 telomeres plots). Range of the subtelomeric domains (SubTel) is indicated with a solid gray line,
703 EARs are indicated with an orange line. **(c)** Genome-wide bootstrap distributions of fold-
704 enrichment (32 × 20-kb windows; n = 1,000 resamples; see Methods: Bootstrapping plots). Gray
705 dashed line is genome average. Black lines show medians and 95% CIs; orange/red circles mark
706 the observed mean in the last 20 kb. Two-sided empirical test with Benjamini-Hochberg (BH)
707 correction, effect sizes via Cohen's d (negative = depletion at ends relative to the genome-wide

null): Hop1 ($p = 0.001$; BH = 0.0015; $d = -3.51$); Red1 ($p < 1x10^{-6}$; BH < 1×10^{-6}; $d = -5.23$); Rec8 ($p = 0.368$; BH = 0.368; $d = -0.89$). **(d)** Metaplots anchored at X elements, stratified by end class. Only fully annotated X elements were used (X-only, n = 7; XY′, n = 20). Flanks scaled to element length (X: 100% each side). Gray dashed line is genome average, vertical dotted lines mark X boundaries; shaded bands indicate 95% confidence intervals (CI; see Methods: Meta gene analyses, and meta-X and Y' elements plots). **(e)** Axis protein ChIP signal (Hop1, Red1, Rec8) at X elements on X-only versus XY′ ends. Values represent the mean ChIP/input signal per X element. Box-and-whisker plots show the distribution across elements. Two-sided unpaired Student's t-tests with BH correction; stars reflect BH-adjusted p (* ≤ 0.05; n.s., not significant). Statistics (per X element; Cohen's d; positive = higher at X-only): Hop1 ($p = 0.0186$; BH = 0.0186; $d = 1.13$); Red1 ($p = 0.0058$; BH = 0.0118; $d = 1.77$); Rec8 ($p = 0.0079$; BH = 0.0118; $d = 1.62$). **(f)** Metaplot anchored at Y′ elements. Only fully annotated Y′ were analyzed and flanks were scaled to 50% of Y′ length. Blue arrow indicates Y′-ORF orientation. Gray dashed line is genome average and vertical dotted lines mark Y′ boundaries. Shaded bands are 95% CIs (see Methods: Meta gene analyses, and meta-X and Y' elements plots). Averages of two biological replicates.

Figure 2: Axis-protein depletion near telomeres is encoded in *cis*.

(a) Schematic showing the analyzed fusion chromosomes derived either from S288c or SK1 [39]. The subtelomeric sequences eliminated as part of the fusion process are indicated by grey bars, and the fusion sites, X and Y' elements are marked. **(b)** Red1 binding (T = 4h) along telomere-proximal arms in SK1/S288C hybrids (chrIV-R and chrI-L), using data from [39]. Tracks are shown for unfused (WT) and chrIV/I fused strains homozygous (hom.) or heterozygous (het) for the fused chromosomes with either *CEN1* or *CEN4* deleted (colors as indicated). Vertical dashed black line indicates engineered fusion sites. The plot only includes points common to all datasets, which is why the WT unfused data in the regions between the telomeres and the fusion sites are missing. Thin lines are genome-normalized Red1 tracks; thick lines are loess-smoothed overlays for trends

734 (span = 1). Circle indicates *CEN1*. The dip in signal on the right side of chrI-L is because of
735 deletion of *CEN1* in some of the strains as previously described [39]. (**c**) Example distance-from-
736 telomere plots showing Red1 ChIP/Input signal along 3 matching chromosome arms in WT
737 SK1/S288c hybrid strains, carrying a haploid genome of SK1 and a haploid genome of S288c [39].
738 SK1 and S288c sequences are sufficiently different that about 25% of reads can be assigned to
739 one of the two genomes [36]. Red1 profiles were manually aligned to show that the offset caused
740 by differences in Y' elements and other subtelomeric sequences does not greatly alter the relative
741 distribution or height of Red1 peaks. **(d)** Coding density versus distance from telomeres overlaid
742 on a metaplot of Red1 enrichment. Graph points show mean coding density in 10-kb bins, plotted
743 at bin midpoints (right y-axis). Error bars are standard deviation. Line connects the dots for easier
744 visualization of trend. Y' elements are included and are responsible for the uptick in signal in
745 coding density in the most telomere-proximal bin.
746
747 **Figure 3: Differential recruitment of Red1 at chromosome ends by Rec8-dependent and**
748 **Rec8-independent pathways.**
749 **(a)** Distance-from-telomere profiles of Red1 (spike-in normalized; see Methods) in WT, *rec8*,
750 *hop1-phd*, and *hop1-phd rec8* during early prophase I (T = 3h) using published data [13,15] (see
751 Methods: Distance from telomeres plots). Colored dashed lines indicate each strain's genome-
752 wide mean after spike-in scaling. Ranges of subtelomeric domains (gray) and EARs (orange) are
753 indicated above the plot. **(b)** Genome-wide bootstrap distributions of fold-enrichment (32 × 20-kb
754 windows; n = 1,000 resamples; see Methods: Bootstrapping plots). Black lines show medians
755 and 95% CIs; orange/red circles mark the observed means in the last 20 kb. Two-sided empirical
756 tests with BH correction; Cohen's d (negative = depletion at ends): WT ($p < 1x10^{-6}$; BH $< 1x10^{-6}$;
757 d = −5.23); *hop1-phd* ($p < 1x10^{-6}$; BH $< 1x10^{-6}$; d = −7.85); *rec8* (p = 0.001; BH = 0.0013; d =
758 3.54); *hop1-phd rec8* (p = 0.059; BH = 0.059; d = 1.87). **(c-d)** Meta-X and Y' elements plots at
759 chromosome ends. X elements were stratified by end class and only fully annotated X elements

760 were used (X-only, n = 7; XY′, n = 20) with flanks scaled to 100% of X length. Y′ elements use
761 flanks scaled to 50% of Y′ length. Blue arrow indicates Y′-ORF orientation. Shaded bands show
762 two-sided 95% CIs (see Methods: Meta gene analyses, and meta-X and Y' elements plots).
763 Averages of two biological replicates.

764

765 **Figure 4: Dot1 shapes axis-protein distribution at chromosome ends and chromosome**
766 **interiors.**

767 **(a)** Mean Red1 vs Rec8 enrichment at Rec8 peaks, split by region (terminal 20 kb, centromeres
768 ±10 kb, interior) using published data [16]. Global fit (purple) and region-specific fits (green dashes).
769 Slope comparisons (two-sided Student's t-tests; BH-adjusted): interior vs telomeres ($p = 3.43 \times 10^{-}$
770 ^{19}; BH = 5.14×10^{-19}); interior vs pericentromeres ($p = 3.12 \times 10^{-24}$; BH = 9.36×10^{-24}); telomeres vs
771 pericentromeres (p = 0.525; BH = 0.525). Stars denote BH-adjusted p-values (*** ≤ 0.001; n.s.,
772 not significant) (See Methods: Quantification of Red1 and Rec8 signals). **(b)** Mean enrichment of
773 H4K44ac and H3K56ac [44], H3K4me3 [45], and H3K79me3 versus distance from telomeres, each
774 normalized to H3 or H4 (see Methods: Distance from telomeres plots). **(c)** Spike-in–normalized
775 Red1 distance profiles in WT, *dot1Δ*, and *set1Δ*. Data from [36]. See Methods: Distance from
776 telomeres plots. Note that *set1Δ* mutants are somewhat less synchronous because of delays in
777 premeiotic DNA replication. **(d-e)** Meta-X and Y' elements plots of Red1 enrichment in WT (red),
778 *dot1Δ* (yellow) and *set1Δ* mutants (purple). X elements stratified by end class and only fully
779 annotated X elements were used (X-only, n = 7; XY′, n = 20) with flanks scaled to 100% of X
780 length. Y′ elements use flanks scaled to 50% of Y′ length. Blue arrow indicates Y′-ORF orientation.
781 Shaded bands show two-sided 95% CIs (see Methods: Meta gene analyses, and meta-X and Y'
782 elements plots). **(f)** Region-stratified Red1 enrichment profiles in WT (pink) and *dot1Δ* mutants
783 (yellow) across intergenic (left) and genic (right) sequences versus distance from telomeres.
784 Averages of two biological replicates.

785

786 **Figure 5: H3K79-independent activity of Dot1 reduces axis proteins near chromosome**
787 **ends.**
788 **(a)** Distance-from-telomere profiles of Red1 enrichment (spike-in normalized) in WT, *dot1Δ,* and
789 *hht1/2-K79R* during early prophase I (T=3h; see Methods: Distance from telomeres plots). WT
790 and *dot1Δ* data are the same as in **Fig. 4c**. **(b)** Genome-wide bootstrap distributions (32 × 20-kb
791 windows; n = 1,000 resamples) of Red1 enrichment. Black lines show medians and two-sided
792 95% CIs; orange/red circles mark the observed mean in the terminal 20 kb. Two-sided empirical
793 test, with BH correction; effect sizes via Cohen's d: WT (p = 0.0020; BH = 0.0030; d = −4.09);
794 *dot1Δ* (p = 0.180; BH = 0.180; d = −1.30); *hht1/2-K79R* (p = 0.0010; BH = 0.0030; d = −6.24). **(c-**
795 **d)** Meta-X and Y' elements plots at chromosome ends. X elements stratified by end class and
796 only fully annotated X elements were used (X-only, n = 7; XY′, n = 20) with flanks scaled to 100%
797 of X length. Y′ elements use flanks scaled to 50% of Y′ length. Blue arrow indicates Y′-ORF
798 orientation. Shaded bands show two-sided 95% CIs (see Methods: Meta gene analyses, and
799 meta-X and Y' elements plots). Averages of two biological replicates.
800
801 **Figure 6: Effects of Dot1 on axis-protein deposition depend on Sir3.**
802 **(a)** Distance-from-telomere profiles of Red1 enrichment (spike-in normalized) in WT, *dot1Δ*, *sir3*,
803 and *sir3 dot1Δ* during early prophase I (T = 3h; see Methods: Distance from telomeres plots). **(b)**
804 Genome-wide bootstrap distributions (32 × 20-kb windows; n = 1,000 resamples) of Red1
805 enrichment. Black lines show medians and two-sided 95% CIs; orange/red circles mark the
806 observed mean in the terminal 20 kb. Two-sided empirical test, with BH correction; effect sizes
807 via Cohen's d: WT (p = 0.002; BH = 0.003; d = −4.09); *dot1Δ* (p = 0.18; BH = 0.18; d = −1.30);
808 *sir3* (p = 0.001; BH = 0.002; d = −5.87); *sir3 dot1Δ* (p = 0.001; BH = 0.002; d = −6.50). **(c-d)** Meta-
809 X and Y' elements plots at chromosome ends. X elements stratified by end class and only fully
810 annotated X elements were used (X-only, n = 7; XY′, n = 20) with flanks scaled to 100% of X
811 length. Y′ elements use flanks scaled to 50% of Y′ length. Blue arrow indicates Y′-ORF orientation.

812 Shaded bands show two-sided 95% CIs (see Methods: Metagene analyses, and meta-X and Y'
813 elements plots). Averages of two biological replicates.
814
815 **Figure 7: Sir3 occupancy relates to local transcription and MNase accessibility near**
816 **chromosome ends.**
817 **(a)** Metaplots anchored at X elements, stratified by end class, and only fully annotated X elements
818 were used (X-only, n = 7; XY′, n = 21). Flanks scaled to element length (X: 100% each side).
819 Vertical dotted lines mark X boundaries. Shaded bands indicate 95% CIs (see Methods:
820 Metagene analyses, and meta-X and Y' elements plots). **(b)** Sir3 ChIP signal at X elements on X-
821 only versus XY′ ends during mid-log, meiotic induction (T = 0h), and meiotic prophase (T = 3h).
822 Values represent the mean ChIP/input signal per X element. Box-and-whisker plots show the
823 distribution across elements. Two-sided unpaired Student's t-tests with BH correction; stars reflect
824 BH-adjusted p (** ≤ 0.01). Statistics (per X element; Cohen's d; negative = lower at XY′): mid-log
825 (p = 0.007; BH = 0.007; d = −1.22); T = 0h (p = 0.007; BH = 0.007; d = −1.32); T = 3 h (p = 0.002;
826 BH = 0.006; d = −1.11). **(c)** Metaplot anchored at Y′ elements. Fully annotated Y′ only; flanks
827 scaled to 50% of Y′ length. Vertical dotted lines mark Y′ boundaries. Blue arrow indicates Y′-ORF
828 orientation. Shaded bands show 95% CIs (see Methods: Metagene analyses, and meta-X and Y'
829 elements plots). **(d-e)** Example Sir3 ChIP-seq tracks on chr VII-L and chr VI-L at mid-log and T =
830 3h. Curves show ChIP/Input. Positions of X elements, Y' elements and ORFs are indicated (inset
831 white triangle shows ORF orientation). **(f)** mRNA-seq fold change (*sir3*/WT, log10) at T = 3h
832 versus average Sir3 ChIP enrichment in the 250 bp upstream of ORFs. Blue dots represent
833 measurements within 5 kb of X elements, red dots are measurements in the rest of the genome.
834 Pearson r values are shown. P values are based on Fisher's r-to-z transformation and two-sided
835 z-test. **(g)** MNase-seq fragment frequency (RPM/kb) at T = 3h versus distance from telomeres
836 (0–40 kb) for WT, *dot1Δ*, *sir3*, and *sir3 dot1Δ.* All experiments: averages of two biological
837 replicates.

838

839 **Figure 8: Sir influences DSB formation near chromosome ends.**

840 **(a)** Boxplots of log10 Spo11-oligo signal (hits per million) at X and Y′ elements in WT and *sir2Δ*,
841 from published datasets [19,73]. Points are element scores; gray lines connect matched elements
842 across strains. Two-sided Wilcoxon rank-sum tests with BH correction; effect sizes are rank-
843 biserial r (positive = higher in *sir2Δ*). X elements: ($p = 7.9x10^{-4}$, $BH = 1.6x10^{-3)}$; r = 0.83), Y′
844 elements: (p = 0.127; BH = 0.127; r = 0.32). Stars reflect BH-adjusted p (** ≤ 0.01; n.s., not
845 significant). **(b)** TrAEL-seq hotspot intensity per 5-kb bin as a function of distance from X
846 elements. Log10 average peak intensity (RPM) for peaks in each bin in *dmc1Δ*, *sir3 dmc1Δ, dot1Δ*
847 *dmc1Δ*, and *sir3 dot1Δ dmc1Δ* (see Methods: TrAEL-seq hotspot calling and quantification). Per-
848 bin two-sided Wilcoxon rank-sum tests contrasting (*sir3 dmc1Δ* + *sir3 dot1Δ dmc1Δ*) vs (*dmc1Δ*
849 + *dot1Δ dmc1Δ*), BH-corrected across bins; effect sizes are rank-biserial (positive = higher in *sir3*
850 mutants. Bin 1: p = 3.15 x 10-7; BH = 1.26 x 10-6; r = 0.67. Bin 2: p = 0.237; BH = 0.474; r = 0.13.
851 Bin 3: p = 0.527; BH = 0.703; r = 0.07. Bin 4: p = 0.823; BH = 0.823; r = 0.02. Stars reflect BH-
852 adjusted p (*** ≤ 0.001; n.s., not significant). **(c)** Mean hotspot counts per 5-kb bin as a function
853 of distance from X elements for the indicated strains. Hotspots were identified from TrAEL-seq
854 peak calls. Because most telomere-proximal bins contained only 0-2 hotspots, the data had too
855 few discrete steps for box or violin plots. Therefore, the means of the data are shown as a bar
856 plot (error bars: SEM). Per-bin two-sided Wilcoxon rank-sum tests contrasting (*sir3 dmc1Δ* + sir3
857 *dot1Δ dmc1Δ*) vs (*dmc1Δ* + *dot1Δ dmc1Δ*), BH-corrected across bins; effect sizes are rank-
858 biserial (positive = higher in *sir3* mutants. Bin 1: raw $p = 5.63x10^{-3}$; $BH = 2.25x10^{-2}$; r = 0.24. Bin
859 2: raw p = 0.376; BH = 0.752; r = 0.08. Bin 3: raw p = 0.687; BH = 0.915; r = 0.04. Bin 4: raw p =
860 0.920; BH = 0.920; r = 0.01. Stars reflect BH-adjusted p (* ≤ 0.05; n.s., not significant). **(d)** TrAEL-
861 seq (colored) and MNase-seq (gray) tracks at a representative subtelomeric region (chrV-R) for
862 *dmc1Δ*, *sir3 dmc1Δ, dot1Δ dmc1Δ*, and *sir3 dot1Δ dmc1Δ*. Black arrow indicates a cryptic DSB
863 hotspot that becomes active in the absence of *SIR3*. Gray arrow indicates an unusual Y'-

associated hotspot that becomes stronger in the absence of *SIR3.* Other Y' elements generally do not exhibit altered TrAEL-seq signal. **(e)** TrAEL-seq meta-plots showing mean DSB signal (reads per million) as a function of distance from X elements in the strains indicated. Ranges of subtelomeric domains (gray) and EARs (orange) are indicated above the plot.

Figure 9: Differential regulation of axis protein deposition near telomeres

Schematic depicting a model of how axis protein recruitment is regulated in the chromosome interior (left) and near chromosome ends (right). Axis protein recruitment occurs in parallel through recruitment by Rec8 cohesin (likely via binding to Red1) and through nucleosome binding by the Hop1 chromatin binding region (CBR). Both recruitment pathways are active near telomeres. Dot1 downmodulates Rec8-dependent recruitment, thereby preventing a positive effect of Sir3. In addition, *cis*-encoded features contribute to reduced axis protein binding near telomeres.

References:

1 Mozzachiodi, S. & Liti, G. Evolution of yeast hybrids by aborted meiosis. *Current Opinion in Genetics and Development* **77**, 101980-101980 (2022). https://doi.org/10.1016/j.gde.2022.101980

2 Börner, G. V., Hochwagen, A. & MacQueen, A. J. Meiosis in budding yeast. *Genetics* **225**, 1-33 (2023). https://doi.org/10.1093/genetics/iyad125

3 Duro, E. & Marston, A. L. From equator to pole: Splitting chromosomes in mitosis and meiosis. *Genes and Development* **29**, 109-122 (2015). https://doi.org/10.1101/gad.255554.114

4 Hunter, N. Meiotic recombination: The essence of heredity. *Cold Spring Harbor Perspectives in Biology* **7** (2015). https://doi.org/10.1101/cshperspect.a016618

5 Arter, M. & Keeney, S. Divergence and conservation of the meiotic recombination machinery. *Nature Reviews Genetics* **25**, 309-325 (2024). https://doi.org/10.1038/s41576-023-00669-8

6 Lichten, M. Meiotic chromatin: The substrate for recombination initiation. *Genome Dynamics and Stability* **3**, 165-193 (2008). https://doi.org/10.1007/7050_2008_040

7 Ito, M. & Shinohara, A. Chromosome architecture and homologous recombination in meiosis. *Frontiers in Cell and Developmental Biology* **10**, 1097446 (2022). https://doi.org/10.3389/fcell.2022.1097446

8 Raghavan, A. R. & Hochwagen, A. Keeping it safe: control of meiotic chromosome breakage. *Trends in Genetics* (2024). https://doi.org/https://doi.org/10.1016/j.tig.2024.11.006

9 Zhang, K., Wu, X. C., Zheng, D. Q. & Petes, T. D. Effects of Temperature on the Meiotic Recombination Landscape of the Yeast *Saccharomyces cerevisiae*. *mBio* **8** (2017). https://doi.org/10.1128/mBio.02099-17

10 Mohibullah, N. & Keeney, S. Numerical and spatial patterning of yeast meiotic DNA breaks by Tel1. *Genome Research* **27** (2017). https://doi.org/10.1101/gr.213587.116

11 Pan, J. *et al.* A hierarchical combination of factors shapes the genome-wide topography of yeast meiotic recombination initiation. *Cell* **144**, 719-731 (2011). https://doi.org/10.1016/j.cell.2011.02.009

12 Panizza, S. *et al.* Spo11-accessory proteins link double-strand break sites to the chromosome axis in early meiotic recombination. *Cell* **146**, 372-383 (2011). https://doi.org/10.1016/j.cell.2011.07.003

13 Heldrich, J. *et al.* Two pathways drive meiotic chromosome axis assembly in *Saccharomyces cerevisiae*. *Nucleic Acids Research* **50**, 4545-4556 (2022).

14 Joshi, N., Barot, A., Jamison, C. & Börner, G. V. Pch2 links chromosome axis remodeling at future crossover sites and crossover distribution during yeast meiosis. *PLoS Genetics* **5**, e1000557 (2009). https://doi.org/10.1371/journal.pgen.1000557

15 Milano, C. R. *et al.* Chromatin binding by HORMAD proteins regulates meiotic recombination initiation. *EMBO Journal* **43**, 836-867 (2024). https://doi.org/10.1038/s44318-024-00034-3

16 Sun, X. *et al.* Transcription dynamically patterns the meiotic chromosome-axis interface. *eLife* **4**, 1-23 (2015). https://doi.org/10.7554/eLife.07424

17 Blitzblau, H. G., Bell, G. W., Rodriguez, J., Bell, S. P. & Hochwagen, A. Mapping of Meiotic Single-Stranded DNA Reveals Double-Strand-Break Hotspots near Centromeres and Telomeres. *Current Biology* **17**, 2003-2012 (2007). https://doi.org/10.1016/j.cub.2007.10.066

18 Mancera, E., Bourgon, R., Brozzi, A., Huber, W. & Steinmetz, L. M. High-resolution mapping of meiotic crossovers and non-crossovers in yeast. *Nature* **454**, 479-485 (2008). https://doi.org/10.1038/nature07135

19 Subramanian, V. V. *et al.* Persistent DNA-break potential near telomeres increases initiation of meiotic recombination on short chromosomes. *Nature Communications* **10**, 1-15 (2019). https://doi.org/10.1038/s41467-019-08875-x

20 Barton, A. B., Su, Y., Lamb, J., Barber, D. & Kaback, D. B. A function for subtelomeric DNA in *Saccharomyces cerevisiae*. *Genetics* **165**, 929-934 (2003). https://doi.org/10.1093/genetics/165.2.929

21 Sasaki, M., Lange, J. & Keeney, S. Genome destabilization by homologous recombination in the germ line. *Nature Reviews Molecular Cell Biology* **11**, 182-195 (2010). https://doi.org/10.1038/nrm2849

22 Ross, L. O., Maxfield, R. & Dawson, D. Exchanges are not equally able to enhance meiotic chromosome segregation in yeast. *PNAS* **93** (1996). https://doi.org/10.1073/pnas.93.10.4979

23 Ghosh, S., Feingold, E. & Dey, S. K. Etiology of Down syndrome: Evidence for consistent association among altered meiotic recombination, nondisjunction, and maternal age across populations. *American Journal of Medical Genetics, Part A* **149a**, 1415-1420 (2009). https://doi.org/10.1002/ajmg.a.32932

24 Lamb, N. E., Yu, K., Shaffer, J., Feingold, E. & Sherman, S. L. Association between maternal age and meiotic recombination for trisomy 21. *American Journal of Human Genetics* **76**, 91-99 (2005). https://doi.org/10.1086/427266

25 Louis, E. J. The chromosome ends of *Saccharomyces cerevisiae*. *Yeast* **11**, 1553-1573 (1995). https://doi.org/10.1002/yea.320111604

26 Pryde, F. E., Gorham, H. C. & Louis, E. J. Chromosome ends: all the same under their caps. *Current Opinion in Genetics and Development* **7**, 822-828 (1997). https://doi.org/10.1016/s0959-437x(97)80046-9

27 Fabre, E. & Spichal, M. in *Subtelomeres* (eds Edward J. Louis & Marion M. Becker) 13-37 (Springer Berlin Heidelberg, 2014).

28 Hocher, A. & Taddei, A. Subtelomeres as Specialized Chromatin Domains. *BioEssays* **42** (2020). https://doi.org/10.1002/bies.201900205

29 Brothers, M. & Rine, J. Distinguishing between recruitment and spread of silent chromatin structures in *Saccharomyces cerevisiae*. *eLife* **11**, 1-23 (2022). https://doi.org/10.7554/eLife.75653

30 Hocher, A. *et al.* Expanding heterochromatin reveals discrete subtelomeric domains delimited by chromatin landscape transitions. *Genome Research* **28**, 1852-1866 (2018). https://doi.org/10.1101/gr.236554.118

31 Gerton, J. L. *et al.* Global mapping of meiotic recombination hotspots and coldspots in the yeast *Saccharomyces cerevisiae*. *PNAS* **97**, 11383-11390 (2000). https://doi.org/10.1073/pnas.97.21.11383

32 Buhler, C., Borde, V. & Lichten, M. Mapping meiotic single-strand DNA reveals a new landscape of DNA double-strand breaks in *Saccharomyces cerevisiae*. *PLoS Biology* **5**, 2797-2808 (2007). https://doi.org/10.1371/journal.pbio.0050324

33 Murakami, H. *et al.* Multilayered mechanisms ensure that short chromosomes recombine in meiosis. *Nature* (2020). https://doi.org/10.1038/s41586-020-2248-2

34 D'Angiolo, M. *et al.* Telomeres are shorter in wild *Saccharomyces cerevisiae* isolates than in domesticated ones. *Genetics* **223** (2023). https://doi.org/10.1093/genetics/iyac186

35 Yue, J. X. *et al.* Contrasting evolutionary genome dynamics between domesticated and wild yeasts. *Nature Genetics* **49**, 913-924 (2017). https://doi.org/10.1038/ng.3847

36 Vale-Silva, L. A., Markowitz, T. E. & Hochwagen, A. SNP-ChIP: A versatile and tag-free method to quantify changes in protein binding across the genome. *BMC Genomics* **20**, 1-10 (2019). https://doi.org/10.1186/s12864-018-5368-4

37 Kwapisz, M. & Morillon, A. Subtelomeric Transcription and its Regulation. *Journal of molecular biology* **432**, 4199-4219 (2020). https://doi.org/10.1016/j.jmb.2020.01.026

38 Wellinger, R. J. & Zakian, V. A. Everything you ever wanted to know about *Saccharomyces cerevisiae* telomeres: Beginning to end. *Genetics* **191**, 1073-1105 (2012). https://doi.org/10.1534/genetics.111.137851

39 Luo, J. *et al.* Synthetic chromosome fusion: Effects on mitotic and meiotic genome structure and function. *Cell Genomics* **3** (2023). https://doi.org/10.1016/j.xgen.2023.100439

40 Glynn, E. F. *et al.* Genome-wide mapping of the cohesin complex in the yeast *Saccharomyces cerevisiae*. *PLoS Biology* **2** (2004). https://doi.org/10.1371/journal.pbio.0020259

41 Bausch, C. *et al.* Transcription Alters Chromosomal Locations of Cohesin in *Saccharomyces cerevisiae*. *Molecular and Cellular Biology* **27**, 8522-8532 (2007). https://doi.org/10.1128/MCB.01007-07

42 Ocampo-Hafalla, M. T. & Uhlmann, F. Cohesin loading and sliding. *Journal of Cell Science* **124**, 685-691 (2011). https://doi.org/10.1242/jcs.073866

43 Borde, V. *et al.* Histone H3 lysine 4 trimethylation marks meiotic recombination initiation sites. *EMBO Journal* **28**, 99-111 (2009). https://doi.org/10.1038/emboj.2008.257

44 Hu, J. *et al.* H4K44 Acetylation Facilitates Chromatin Accessibility during Meiosis. *Cell Reports* **13**, 1772-1780 (2015). https://doi.org/10.1016/j.celrep.2015.10.070

45 Zhu, X. & Keeney, S. High-resolution global analysis of the influences of Bas1 and Ino4 transcription factors on meiotic DNA break distributions in *Saccharomyces cerevisiae*. *Genetics* **201**, 525-542 (2015). https://doi.org/10.1534/genetics.115.178293

46 Bani Ismail, M., Shinohara, M. & Shinohara, A. Dot1-dependent histone H3K79 methylation promotes the formation of meiotic double-strand breaks in the absence of histone H3K4 methylation in budding yeast. *PLoS ONE* **9** (2014). https://doi.org/10.1371/journal.pone.0096648

47 Shilatifard, A. Chromatin modifications by methylation and ubiquitination: Implications in the regulation of gene expression. *Annual Review of Biochemistry* **75**, 243-269 (2006). https://doi.org/10.1146/annurev.biochem.75.103004.142422

48 Takahashi, Y.-H. *et al.* Dot1 and Histone H3K79 Methylation in Natural Telomeric and HM Silencing. *Molecular Cell* **42**, 118-126 (2011). https://doi.org/10.1016/j.molcel.2011.03.006

49 Hoppe, G. J. *et al.* Steps in Assembly of Silent Chromatin in Yeast: Sir3-Independent Binding of a Sir2/Sir4 Complex to Silencers and Role for Sir2-Dependent Deacetylation. *Molecular and Cellular Biology* **22**, 4167-4180 (2002). https://doi.org/10.1128/MCB.22.12.4167-4180.2002

50 Rusche, L. N., Kirchmaier, A. L. & Rine, J. The Establishment, Inheritance, and Function of Silenced Chromatin in *Saccharomyces cerevisiae*. *Annual Review of Biochemistry* **72**, 481-516 (2003). https://doi.org/10.1146/annurev.biochem.72.121801.161547

51 Pryde, F. E. & Louis, E. J. Limitations of silencing at native yeast telomeres. *EMBO Journal* **18**, 2538-2550 (1999). https://doi.org/10.1093/emboj/18.9.2538

52 Gartenberg, M. R. & Smith, J. S. The Nuts and Bolts of Transcriptionally Silent Chromatin in *Saccharomyces cerevisiae*. *Genetics* **203**, 1563-1599 (2016). https://doi.org/10.1534/genetics.112.145243

53 Hediger, F., Neumann, F. R., Van Houwe, G., Dubrana, K. & Gasser, S. M. Live imaging of telomeres: yKu and Sir proteins define redundant telomere-anchoring pathways in yeast. *Current Biology* **12**, 2076-2089 (2002). https://doi.org/10.1016/s0960-9822(02)01338-6

54 Mieczkowski, P. A., Dominska, M., Buck, M. J., Lieb, J. D. & Petes, T. D. Loss of a histone deacetylase dramatically alters the genomic distribution of Spo11p-catalyzed DNA breaks in *Saccharomyces cerevisiae*. *PNAS* **104**, 3955-3960 (2007). https://doi.org/10.1073/pnas.0700412104

55 Kara, N., Krueger, F., Rugg-Gunn, P. & Houseley, J. Genome-wide analysis of DNA replication and DNA double-strand breaks using TrAEL-seq. *PLoS Biology* **19** (2021). https://doi.org/10.1371/journal.pbio.3000886

56 Bishop, D. K., Park, D., Xu, L. & Kleckner, N. *DMC1*: A meiosis-specific yeast homolog of E. coli *recA* required for recombination, synaptonemal complex formation, and cell cycle progression. *Cell* **69**, 439-456 (1992). https://doi.org/10.1016/0092-8674(92)90446-J

57 Vader, G. *et al.* Protection of repetitive DNA borders from self-induced meiotic instability. *Nature* **477**, 115-121 (2011). https://doi.org/10.1038/nature10331

58 Blitzblau, H. G., Chan, C. S., Hochwagen, A. & Bell, S. P. Separation of DNA replication from the assembly of break-competent meiotic chromosomes. *PLoS Genetics* **8**, e1002643 (2012). https://doi.org/10.1371/journal.pgen.1002643

59 Stulemeijer, I. J. *et al.* Dot1 binding induces chromatin rearrangements by histone methylation-dependent and -independent mechanisms. *Epigenetics and Chromatin* **4**, 2 (2011). https://doi.org/10.1186/1756-8935-4-2

60 Lee, S. *et al.* Dot1 regulates nucleosome dynamics by its inherent histone chaperone activity in yeast. *Nature Communications* **9**, 240 (2018). https://doi.org/10.1038/s41467-017-02759-8

61 San-Segundo, P. A. & Roeder, G. S. Role for the Silencing Protein Dot1 in Meiotic Checkpoint Control. 3601-3615 (2000).
62 Wood, K., Tellier, M. & Murphy, S. DOT1L and H3K79 Methylation in Transcription and Genomic Stability. *Biomolecules* **8** (2018). https://doi.org/10.3390/biom8010011
63 Mizuno, K. *et al.* The meiotic recombination hot spot created by the single-base substitution ade6-M26 results in remodeling of chromatin structure in fission yeast. *Genes Dev* **11**, 876-886 (1997). https://doi.org/10.1101/gad.11.7.876
64 He, F. *et al.* SESAME-catalyzed H3T11 phosphorylation inhibits Dot1-catalyzed H3K79me3 to regulate autophagy and telomere silencing. *Nature Communications* **13**, 7526 (2022). https://doi.org/10.1038/s41467-022-35182-9
65 Su, Y., Barton, A. B. & Kaback, D. B. Decreased meiotic reciprocal recombination in subtelomeric regions in *Saccharomyces cerevisiae*. *Chromosoma* **109**, 467-475 (2000). https://doi.org/10.1007/s004120000098
66 Humphryes, N. & Hochwagen, A. A non-sister act: Recombination template choice during meiosis. *Experimental Cell Research* **329**, 53-60 (2014). https://doi.org/10.1016/j.yexcr.2014.08.024
67 Scherthan, H. A bouquet makes ends meet. *Nature Reviews Molecular Cell Biology* **2**, 621-627 (2001). https://doi.org/10.1038/35085086
68 Medhi, D., Goldman, A. S. & Lichten, M. Local chromosome context is a major determinant of crossover pathway biochemistry during budding yeast meiosis. *eLife* **5**, e19669 (2016). https://doi.org/10.7554/eLife.19669.001
69 Langmead, B. & Salzberg, S. L. Fast gapped-read alignment with Bowtie 2. *Nature Methods* **9**, 357-359 (2012). https://doi.org/10.1038/nmeth.1923
70 Kar, F. M., Vogel, C. & Hochwagen, A. Meiotic DNA breaks activate a streamlined phospho-signaling response that largely avoids protein-level changes. *Life Science Alliance* **5**, 1-15 (2022). https://doi.org/10.26508/LSA.202201454
71 Ewels, P. A. P. A. F. S. & et al. The nf-core framework for community-curated bioinformatics pipelines. *Nature Biotechnology* **38**, 271-271 (2020). https://doi.org/10.1038/s41587-020-0435-1
72 Patro, R., Duggal, G., Love, M. I., Irizarry, R. A. & Kingsford, C. Salmon provides fast and bias-aware quantification of transcript expression. *Nature Methods* **14**, 417-419 (2017). https://doi.org/10.1038/nmeth.4197
73 Thacker, D., Mohibullah, N., Zhu, X. & Keeney, S. Homologue engagement controls meiotic DNA break number and distribution. *Nature* **510**, 241-246 (2014). https://doi.org/10.1038/nature13120

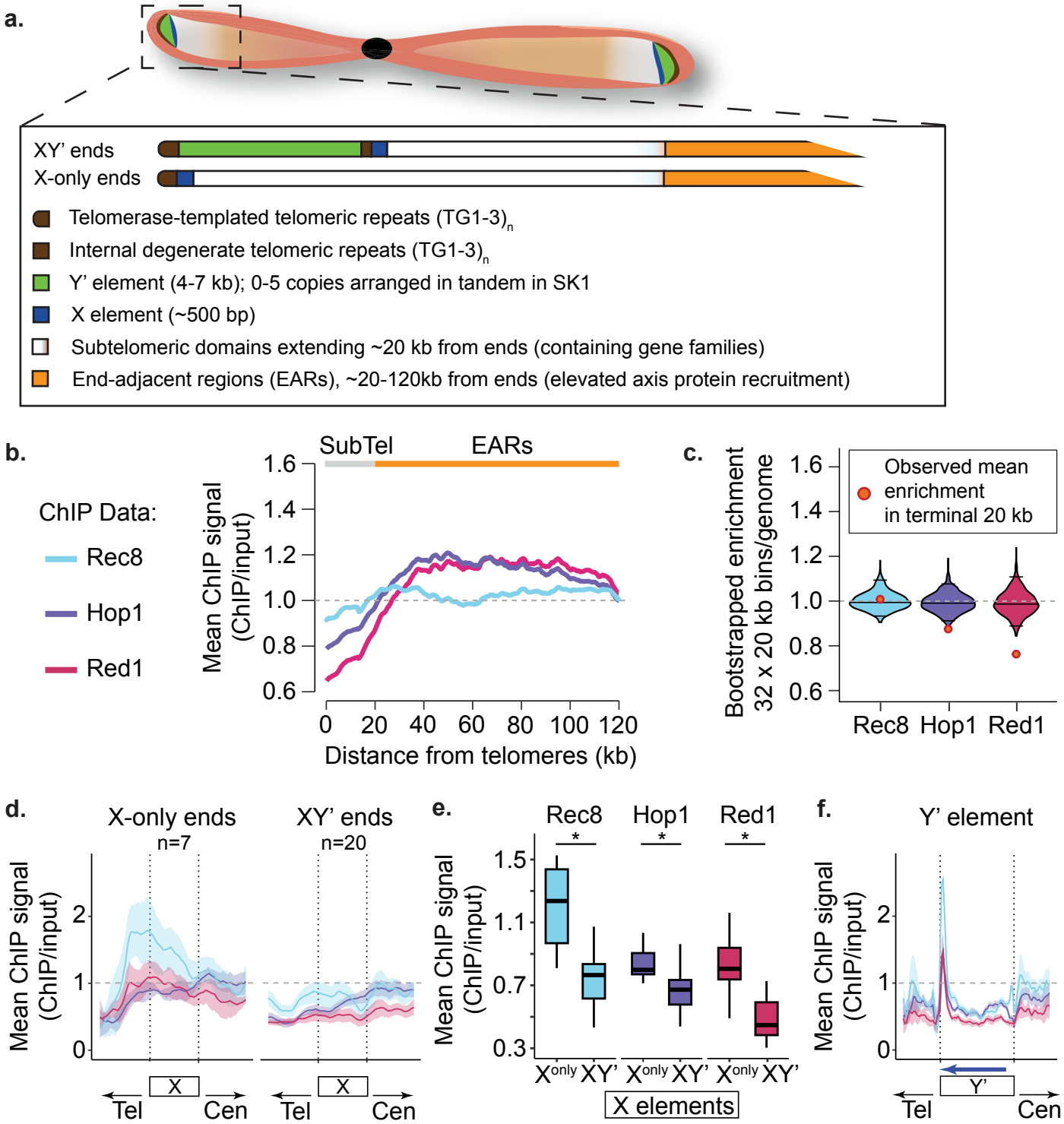

Raghavan *et al*, Fig. 1

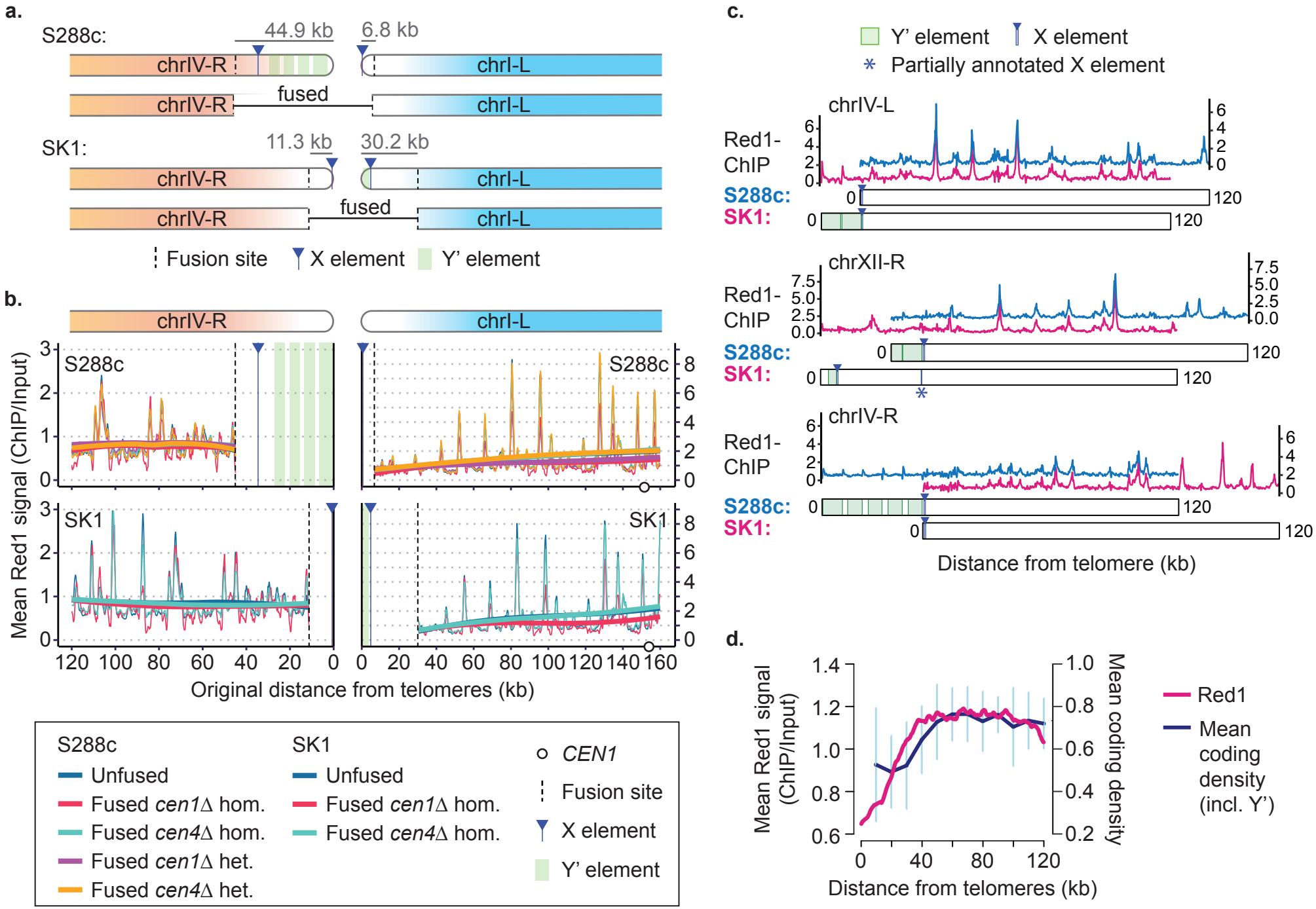
a.
S288c:
44.9 kb
6.8 kb
chrIV-R
chrI-L
fused
SK1:
11.3 kb
30.2 kb
Fusion site
X element
Y' element
b.
S288c
SK1
Mean Red1 signal (ChIP/Input)
Original distance from telomeres (kb)
S288c
Unfused
Fused cen1Δ hom.
Fused cen4Δ hom.
Fused cen1Δ het.
Fused cen4Δ het.
SK1
Unfused
Fused cen1Δ hom.
Fused cen4Δ hom.
CEN1
Fusion site
X element
Y' element
c.
Y' element
X element
Partially annotated X element
chrIV-L
chrXII-R
chrIV-R
Red1-ChIP
S288c:
SK1:
Distance from telomere (kb)
d.
Mean Red1 signal (ChIP/Input)
Mean coding density
Distance from telomeres (kb)
Red1
Mean coding density (incl. Y')

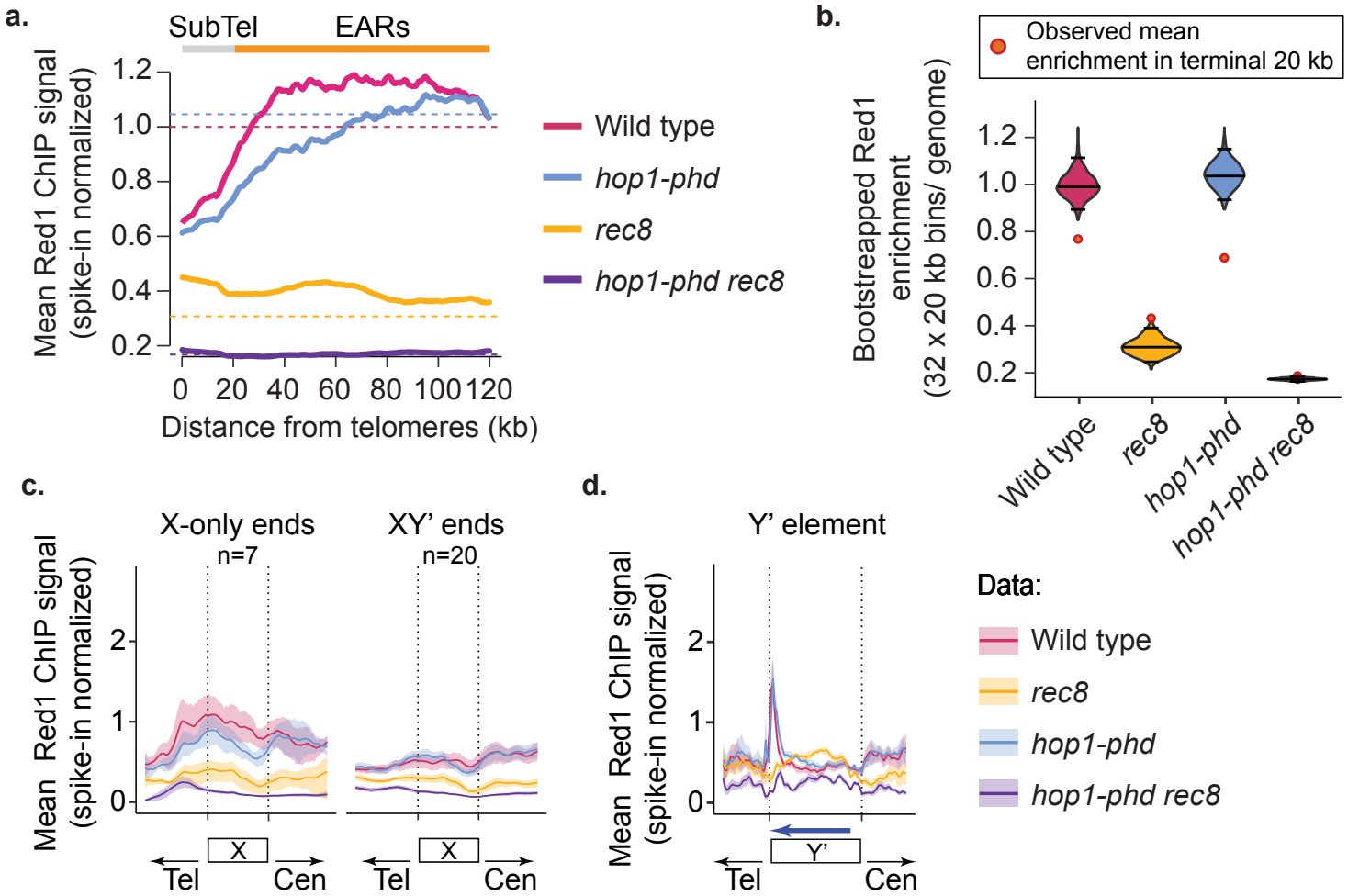

Raghavan *et al*, Fig. 3

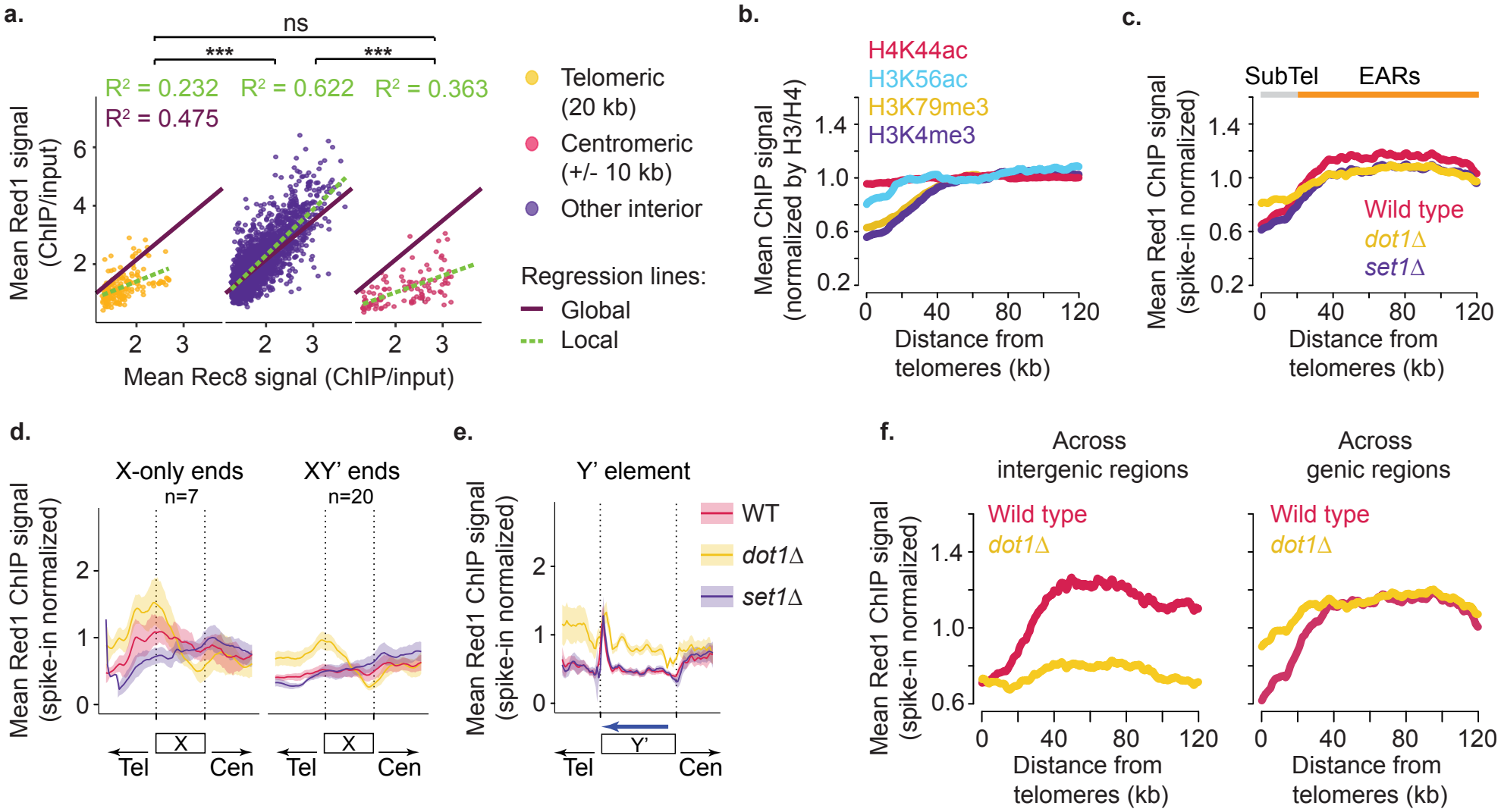

Raghavan *et al*, Fig. 4

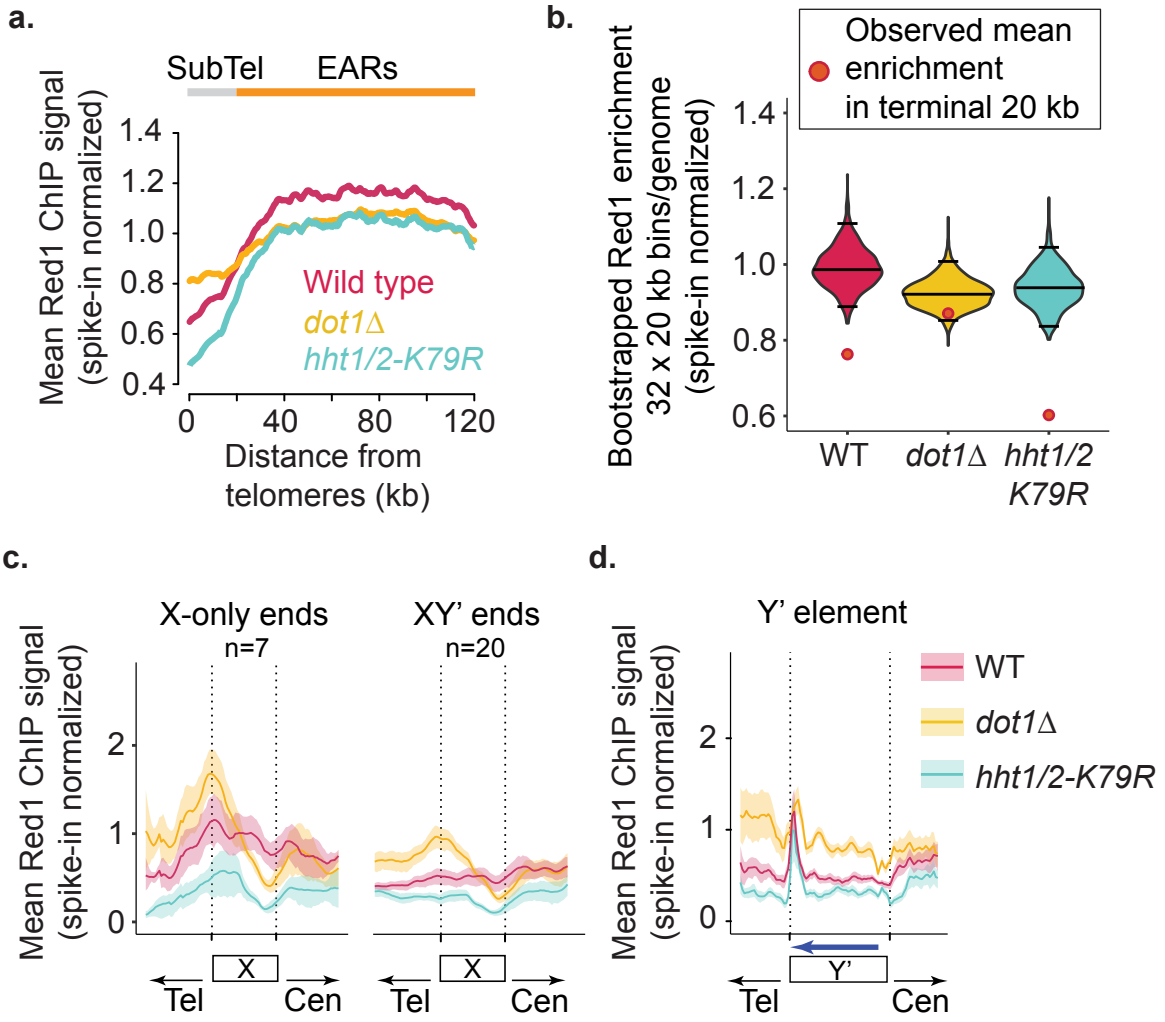

Raghavan *et al*, Fig. 5

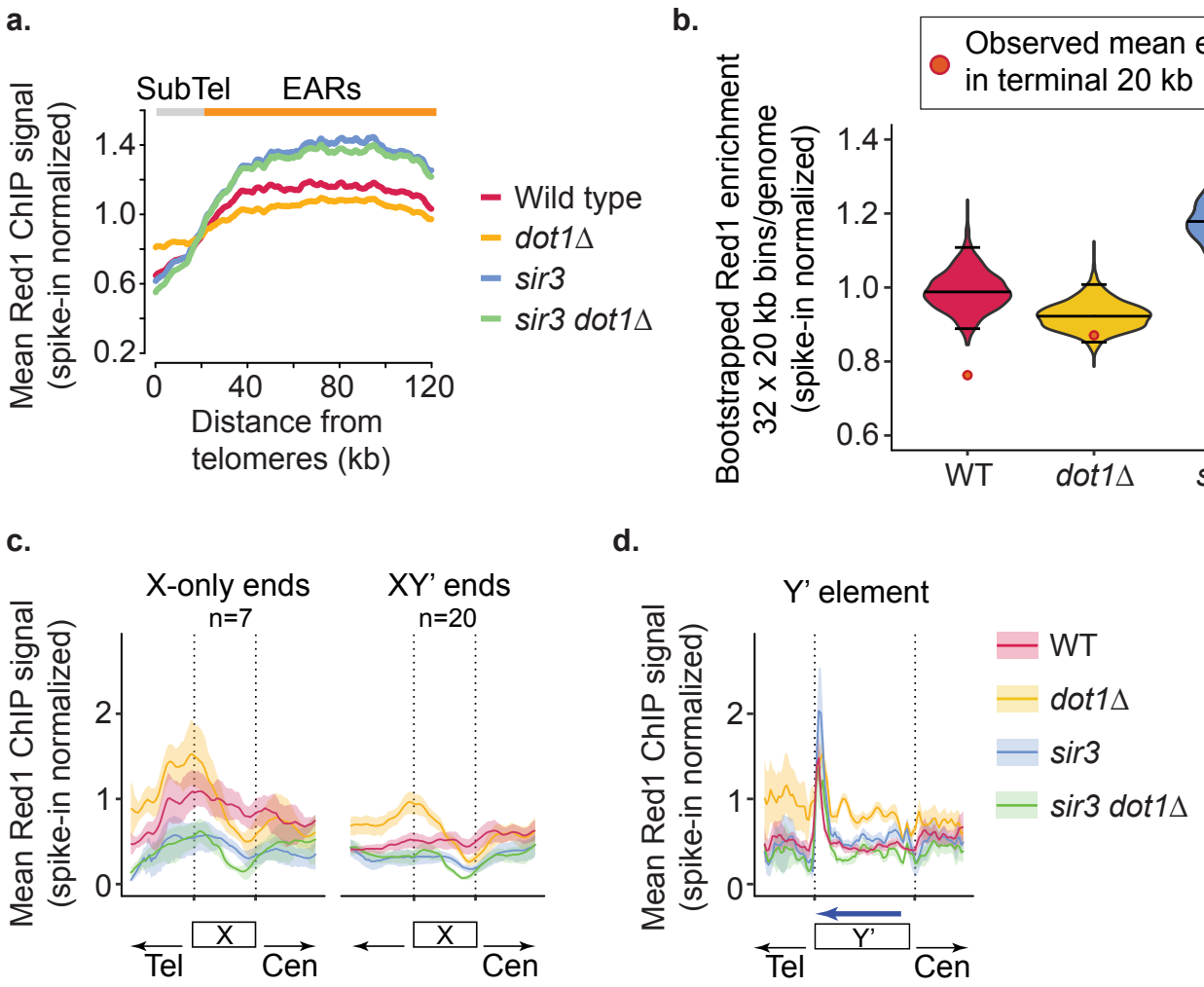

Raghavan *et al*, Figure 6

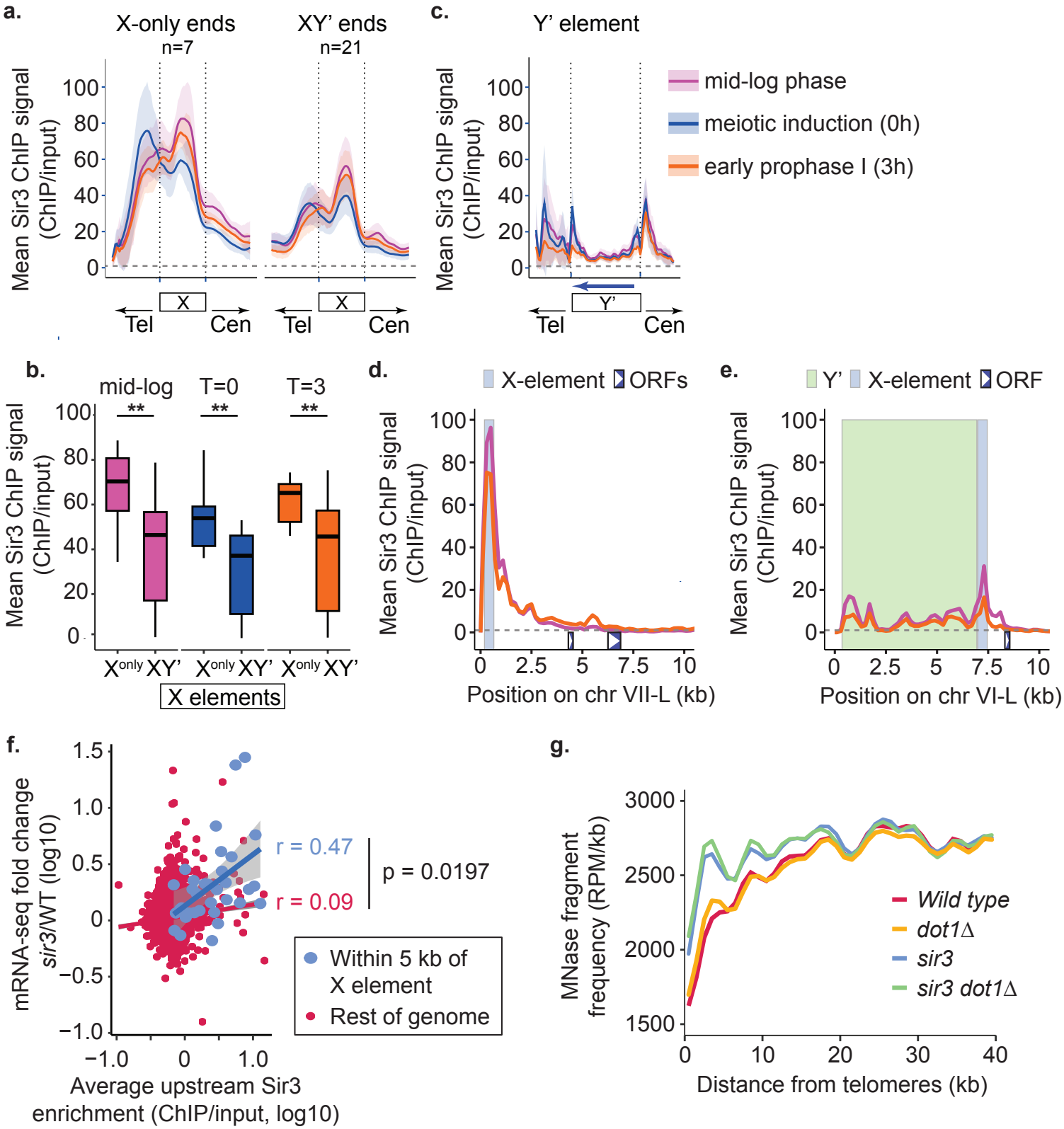

Raghavan *et al*, Fig. 7

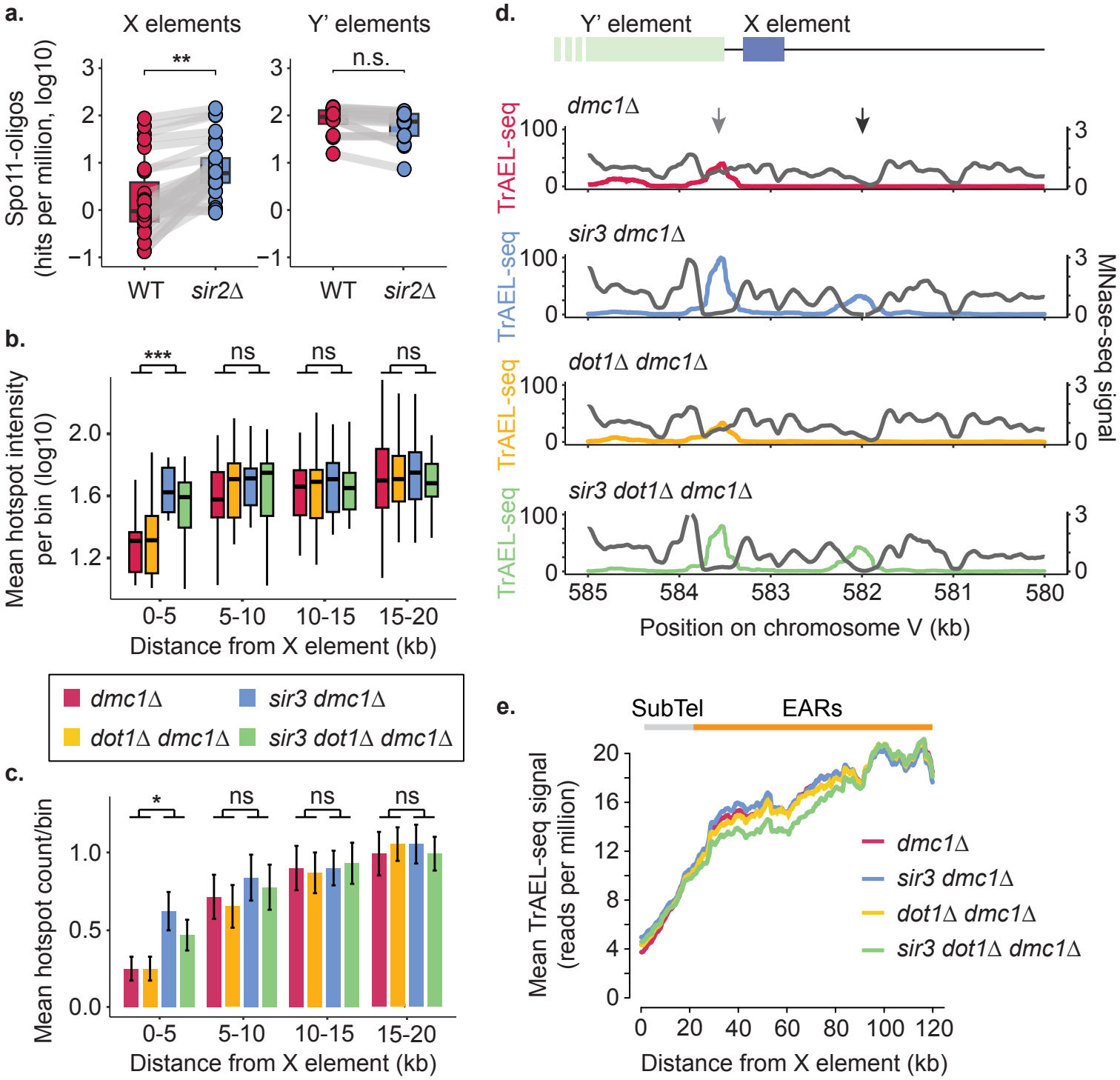

Raghavan *et al*, Fig. 8

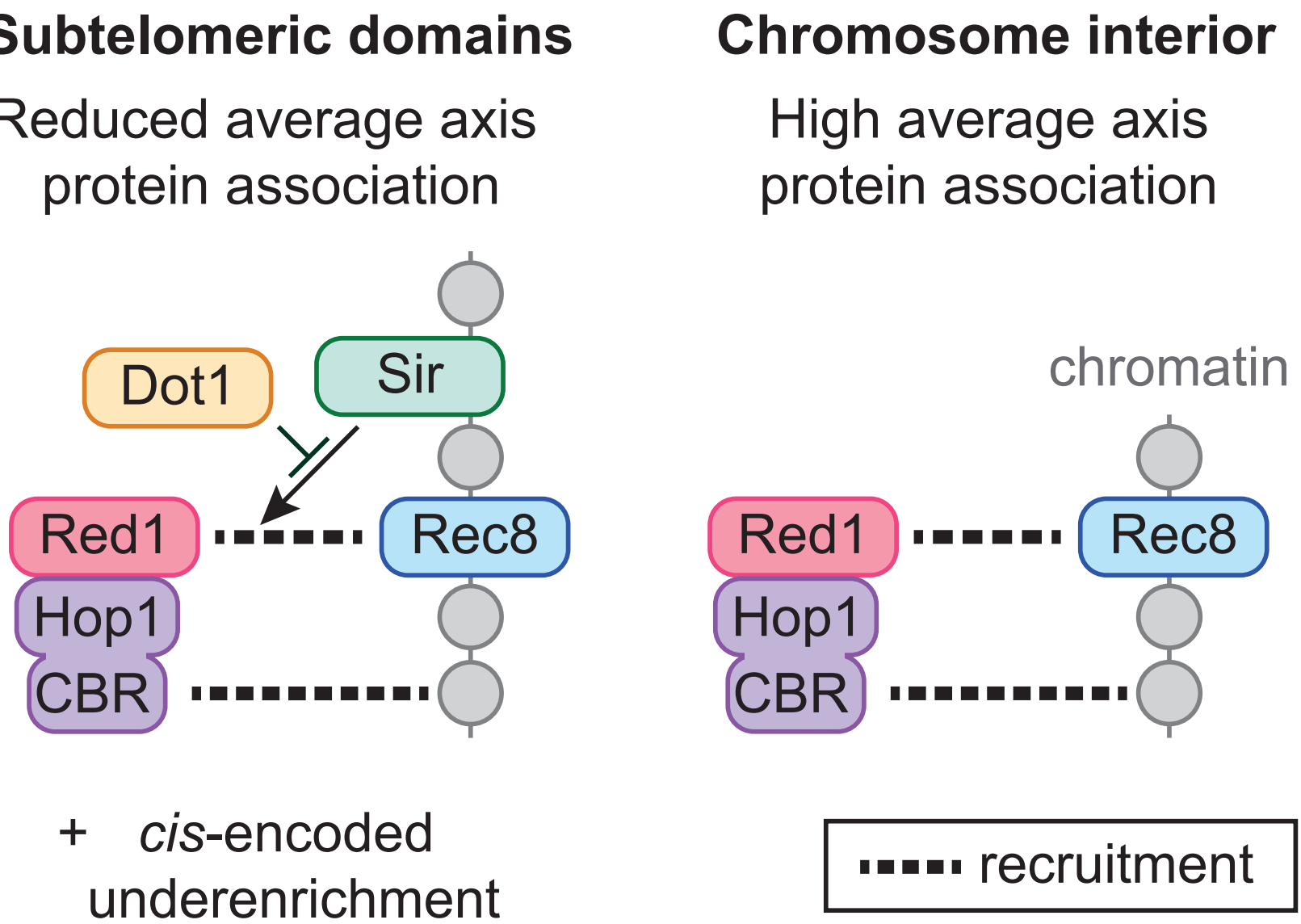
Subtelomeric domains
Reduced average axis protein association
Dot1
Sir
Red1
Rec8
Hop1
CBR
+ *cis*-encoded underenrichment
Chromosome interior
High average axis protein association
chromatin
Red1
Rec8
Hop1
CBR
recruitment

Supplementary Figures:

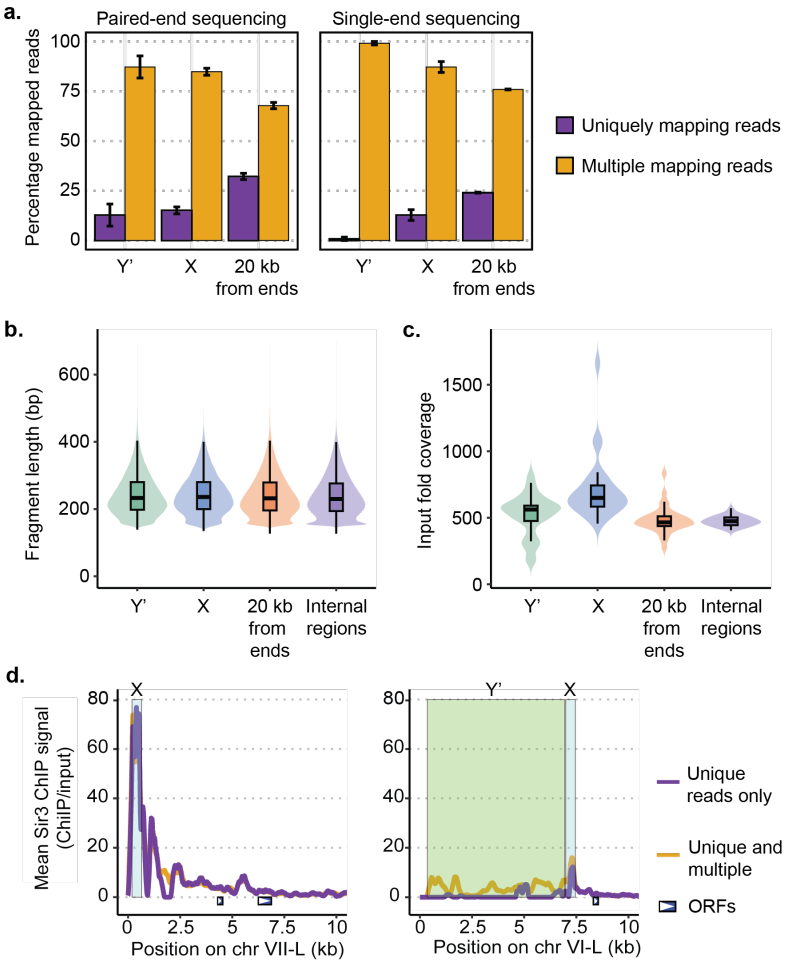

Supplementary Figure 1: Enhanced coverage at chromosome ends with a tailored mapping workflow.

(a) Fraction of uniquely mapping and multiple-mapping reads within Y′ elements, X elements, and the terminal 20-kb (subtelomeric domains), shown for paired-end and single-end libraries. Bars show mean across replicates; error bars, SD. **(b)** Fragment-length distributions for unbiased input DNA in Y′, X, terminal 20 kb, and internal regions. Violin plots show the full distribution of paired fragments. Embedded boxplots mark the median and interquartile range**.** **(c)** Input fold coverage across the same region classes, displayed as violin plots with embedded boxplots. For X, Y′, and terminal 20-kb regions, coverage was calculated as the averaged depth

per element. For internal regions, we averaged depth within non-overlapping 20-kb windows defined after excluding X, Y′, and terminal 20-kb regions. The increased input signal for X elements likely reflects the missing X-element annotations on several chromosomes (**Supplementary Fig. 2**). Since all ChIP profiles are plotted as ChIP/input, any increase in input signal will be mirrored in the ChIP signal and thus will not affect conclusions. **(d)** Sir3 ChIP profiles at representative subtelomeres (chr VII-L; chr VI-L), comparing unique versus unique+multi-mapping pipelines. Shaded rectangles mark X and Y' elements. Blue boxes and arrowheads indicate ORFs and their direction. Values are means of two independent biological replicates and were reproducible across replicates.

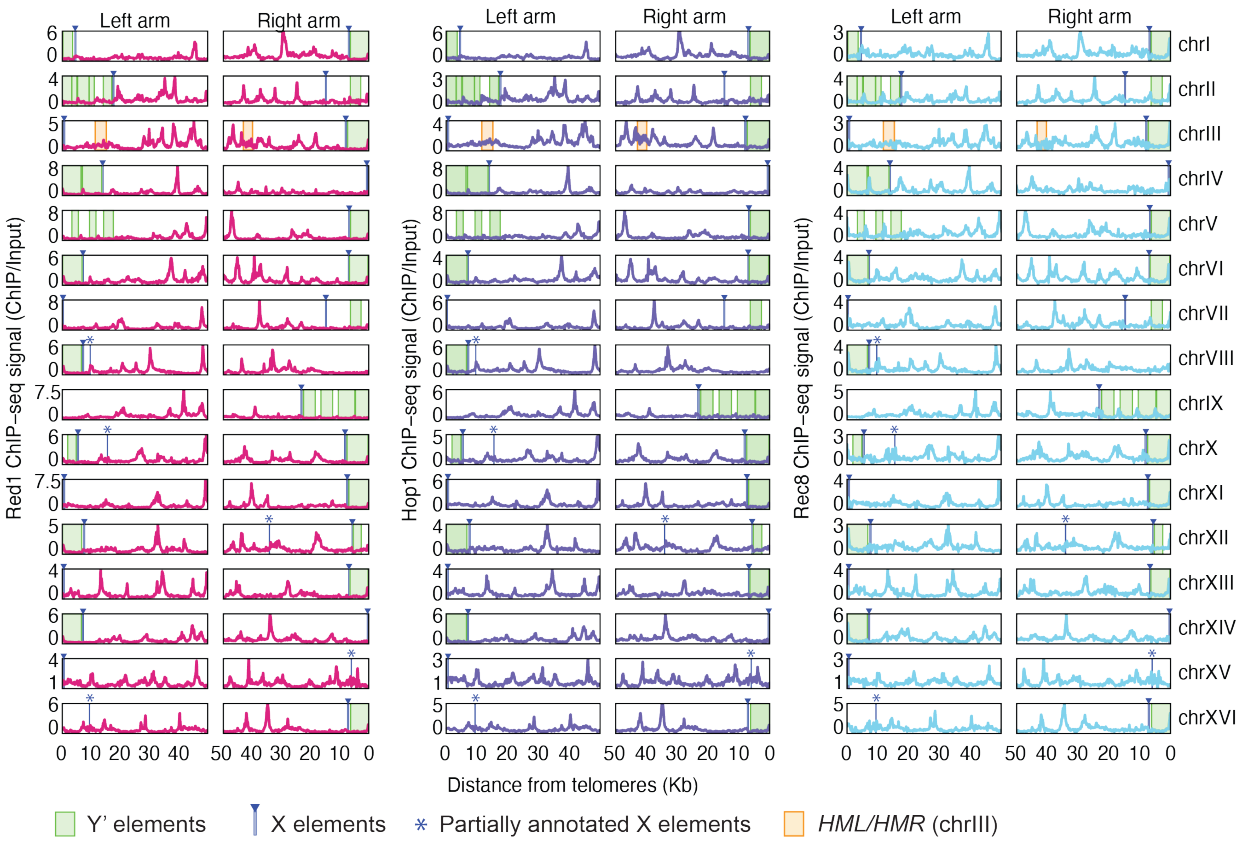

Supplementary Figure 2: Axis-protein ChIP profiles across all chromosome ends. Distance-from-telomere ChIP/Input signal for Red1, Hop1, and Rec8 at every left and right arm (32 ends) in WT early prophase I. Green blocks mark all annotated Y′ elements and blue blocks with arrowheads mark all annotated X-elements (fully and partially annotated copies shown: X, n = 32; Y′, n = 31). The partially annotated copies (marked with stars) are located more internally and are likely an artefact of the incomplete sequence conservation and the small size of X elements. These partially annotated X elements were not used for analyses shown in this study. Signals are from published datasets [1-3]. The positions of the silent mating type loci near the left (*HML*) and right (*HMR*) telomeres of chrIII are also indicated.

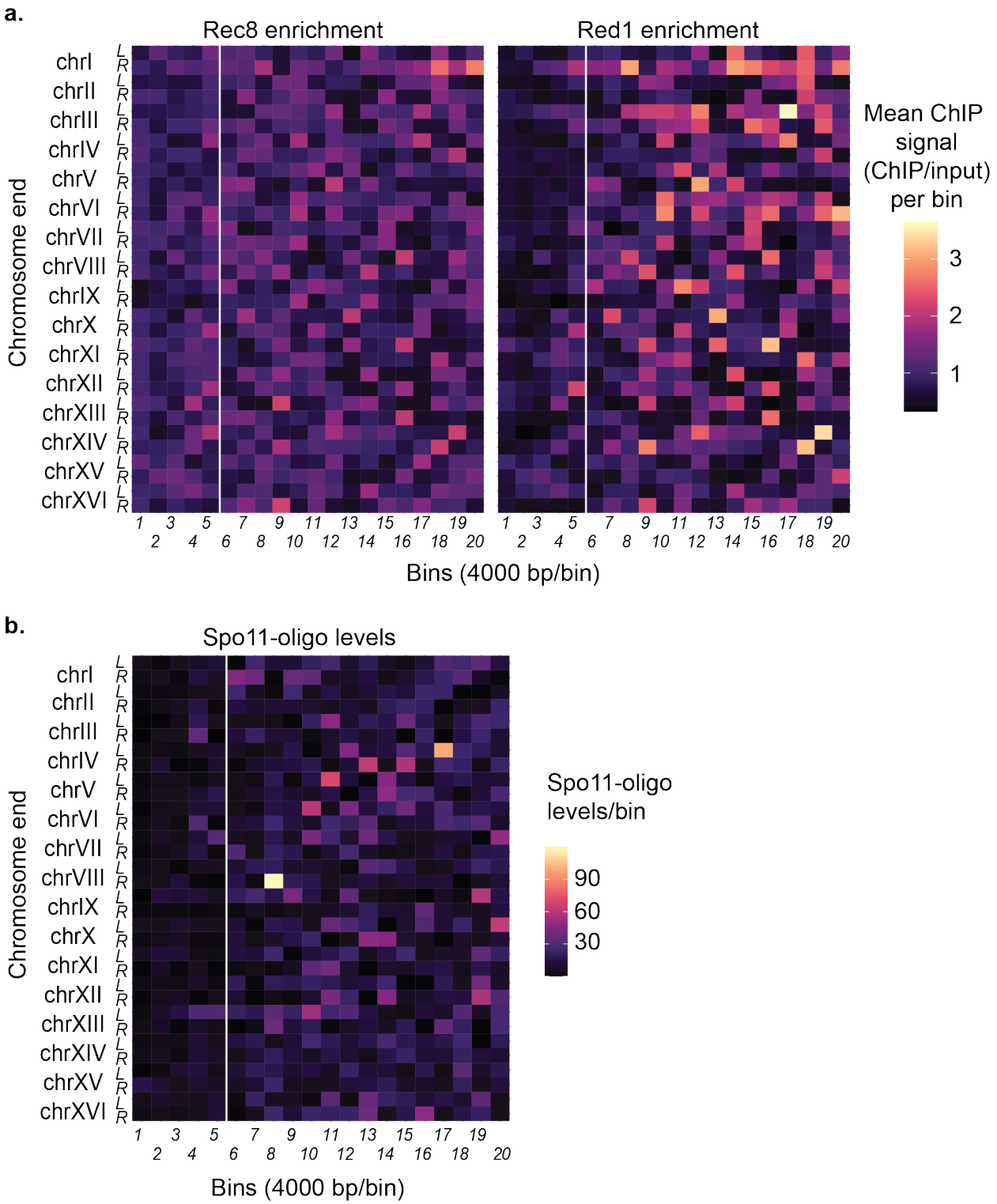

Supplementary Figure 3: Consistent axis-protein and Spo11-oligo depletion across chromosome ends.

(a) Heatmaps of Rec8 and Red1 ChIP enrichment (ChIP/Input) in WT early prophase I (T = 3h) from published data [2,3]. Each row is a chromosome end (left/right indicated). Columns are contiguous 4-kb bins extending inwards from the telomeres. Colors show the mean signal per bin; the vertical white line marks 20 kb from the end. **(b)** Heatmap of Spo11-oligo density (WT; data from [4]) in the same 4-kb binning method. Values are means of two independent biological replicates and were reproducible across replicates.

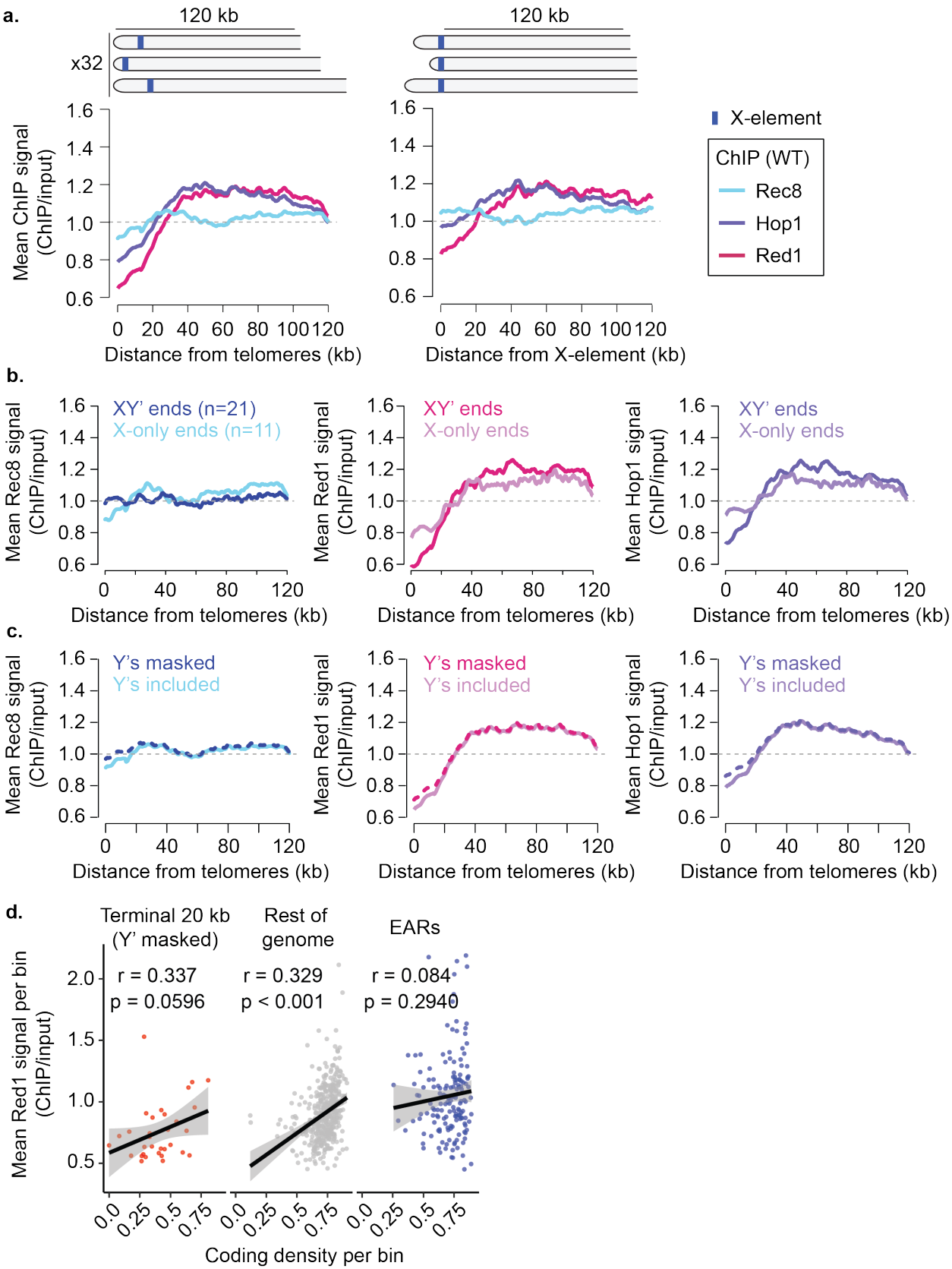
a.
120 kb
x32
120 kb
X-element
ChIP (WT)
Rec8
Hop1
Red1
Mean ChIP signal (ChIP/input)
Distance from telomeres (kb)
Distance from X-element (kb)
b.
XY' ends (n=21)
X-only ends (n=11)
XY' ends
X-only ends
Mean Rec8 signal (ChIP/input)
Mean Red1 signal (ChIP/input)
Mean Hop1 signal (ChIP/input)
Distance from telomeres (kb)
c.
Y's masked
Y's included
d.
Terminal 20 kb (Y' masked)
Rest of genome
EARs
r = 0.337
p = 0.0596
r = 0.329
p < 0.001
r = 0.084
p = 0.2940
Mean Red1 signal per bin (ChIP/input)
Coding density per bin

Supplementary Figure 4: Axis-protein distance profiles using alternative anchors and Y′ masking.

(a) Mean enrichment of Rec8, Red1, and Hop1 (ChIP/Input) in WT early prophase I (T = 3h) from published datasets [1-3], normalized to a genome average of 1 (gray dashed line). Left panel: distance from telomeres; right panel: distance from the annotated X-element anchor. Curves were computed as described in Methods: Distance-from-telomere profiling. **(b)** Distance-from-telomere profiles stratified by end class: XY′ ends (n = 21) versus X-only ends (n = 11) for Rec8, Red1, and Hop1. **(c)** Distance-from-telomere profiles with Y′ elements included (solid) versus masked (dashed). For masking, overlapping annotated Y′ elements were set to NA prior to averaging; all other processing was identical. All values are averages of two biological replicates and were reproducible across replicates. **(d)** Relationship between coding density and mean Red1 enrichment. Scatter plots show non-overlapping 20-kb bins at dots. Black lines are least-squares fits, with 95% CIs shown in gray. Pearson r values are indicated. P values are based on two-sided t-tests on the slope. “Y′ masked” means Y′ sequence is excluded from both measurements (we mask Y′ bases when tallying coding density and when averaging Red1; bins that are entirely Y′ are excluded). Including the Y’ elements eliminated the correlation in the last 20 kb (r = -0.174; p = 0.341).

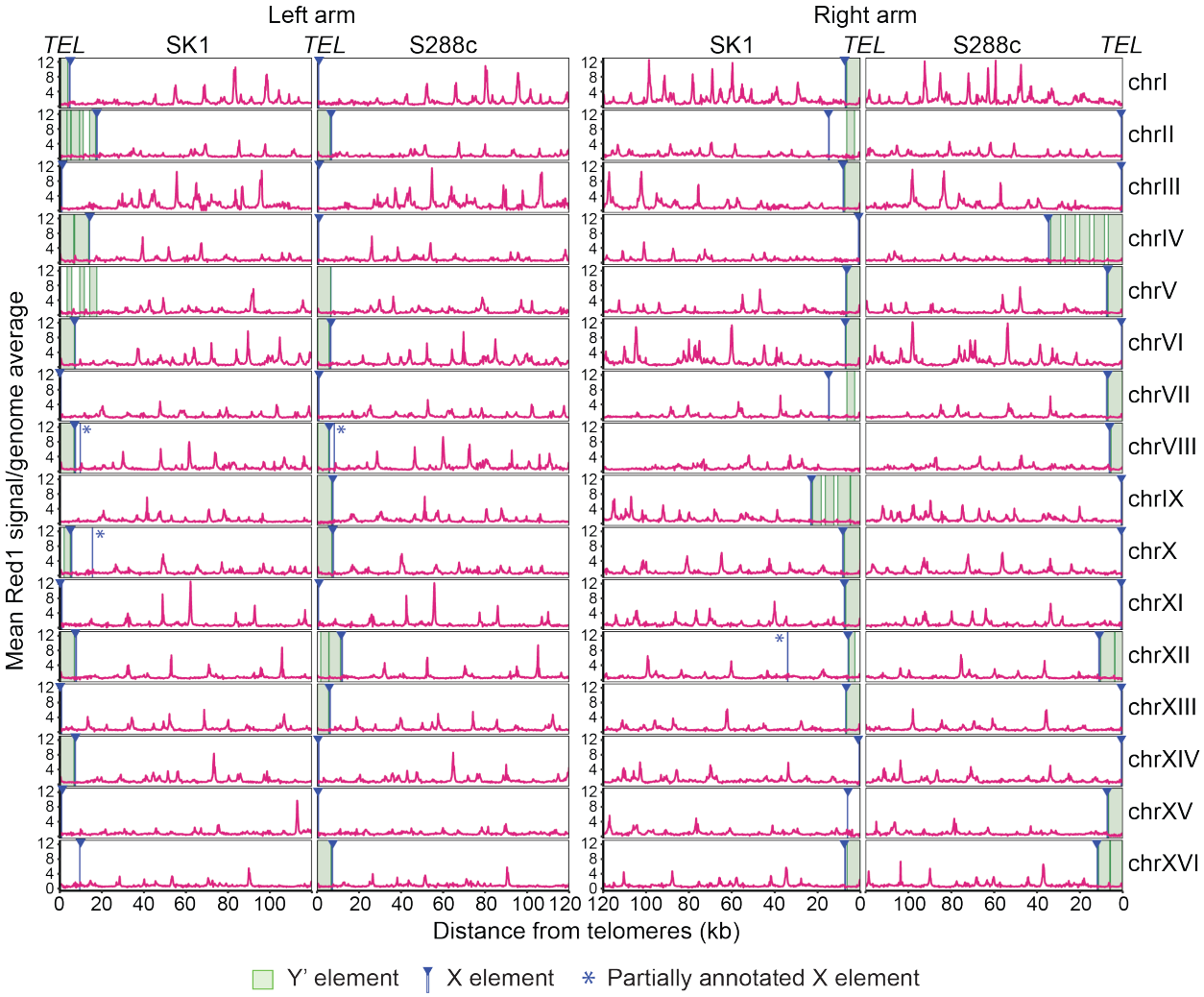

Supplementary Fig. 5: Red1 distribution near chromosome ends in SK1 and S288c. Distance-from-telomere ChIP/Input signal for Red1 (T = 4h) measured in WT SK1/S288c hybrid strains carrying a haploid genome of SK1 and a haploid genome of S288c [5]. The sequences between SK1 and S288c are sufficiently different that about 25% of reads can be assigned to one of the two genomes [3]. The corresponding ends for SK1 and S288c are shown juxtaposed for all 32 ends. Green blocks mark all annotated Y′ elements and blue blocks with arrowheads mark all annotated X-elements. Partially annotated X-elements are marked with stars.

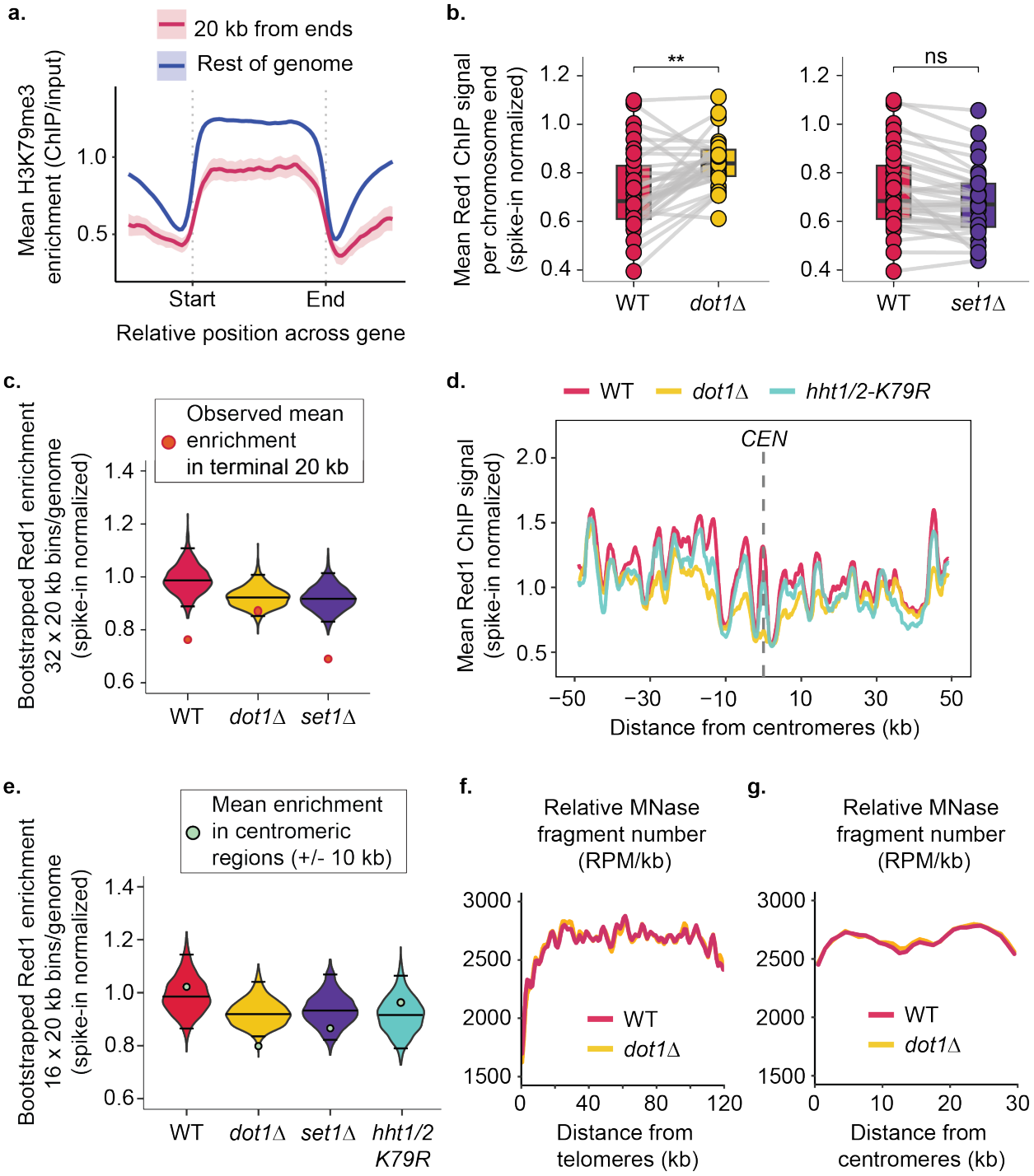

Supplementary Fig. 6: Chromatin features and the role of histone methyltransferases at chromosome ends and centromeres. (a) Meta-ORF profiles of H3K79me3 (normalized to H3) in WT at early prophase I (T = 3h). Curves show mean ChIP/Input with shaded 95% CIs for

genes in the terminal 20 kb (pink) versus the rest of the genome (blue; see Methods: Meta gene analyses, and meta-X and Y' elements plots). **(b)** Mean Red1 signal per chromosome end (terminal 20 kb) in WT, *dot1Δ*, and *set1Δ* using published datasets [2,3]. Points are individual ends. Gray lines connect matched ends across strains. Two-sided Student's *t*-tests with BH correction; effect sizes are Cohen's *d* (positive = higher than WT): *dot1Δ* vs WT (p = 0.0020, BH = 0.0038, d = 0.82); *set1Δ* vs WT (p = 0.181, BH = 0.181, d = 0.34). **(c)** Genome-wide bootstrap distributions of Red1 enrichment (32 × 20-kb windows; n = 1,000 resamples). Black lines mark medians and two-sided 95% CIs; orange/red circles mark the observed mean in the terminal 20 kb (see Methods: Bootstrap test and violin plots). Two-sided empirical tests with BH correction; Cohen's *d* (negative = depletion at ends): WT (p = 0.001, BH = 0.0015, d = −4.15); *dot1Δ* (p = 0.163, BH = 0.163, d = −1.34); *set1Δ* ($p < 1\times10^{-6}$, BH $< 1\times10^{-6}$, d = −4.86). **(d)** Red1 distance-from-centromere profiles (± 50 kb) in WT, *dot1Δ*, and *hht1/2-K79R* (spike-in normalized). Dashed line marks the centromere midpoint. Signals were extracted in 100-bp bins around each centromere. **(e)** Bootstrap test centered on centromeres (± 10 kb; 16 × 20-kb genome windows). Two-sided empirical tests with BH correction; Cohen's *d* (negative = depletion at chromosome ends): WT (p = 0.679, BH = 0.679, d = 0.43); *dot1Δ* (p = 0.020, BH = 0.060, d = −2.44); *set1Δ* (p = 0.253, BH = 0.379, d = −1.12); *hht1/2-K79R* (p = 0.520, BH = 0.679, d = 0.65). **(f-g)** MNase-seq fragment frequency (RPM/kb) versus distance from telomeres **(f)** or centromeres **(g)** in WT and *dot1Δ*. All values are averages of two biological replicates and were reproducible across replicates.

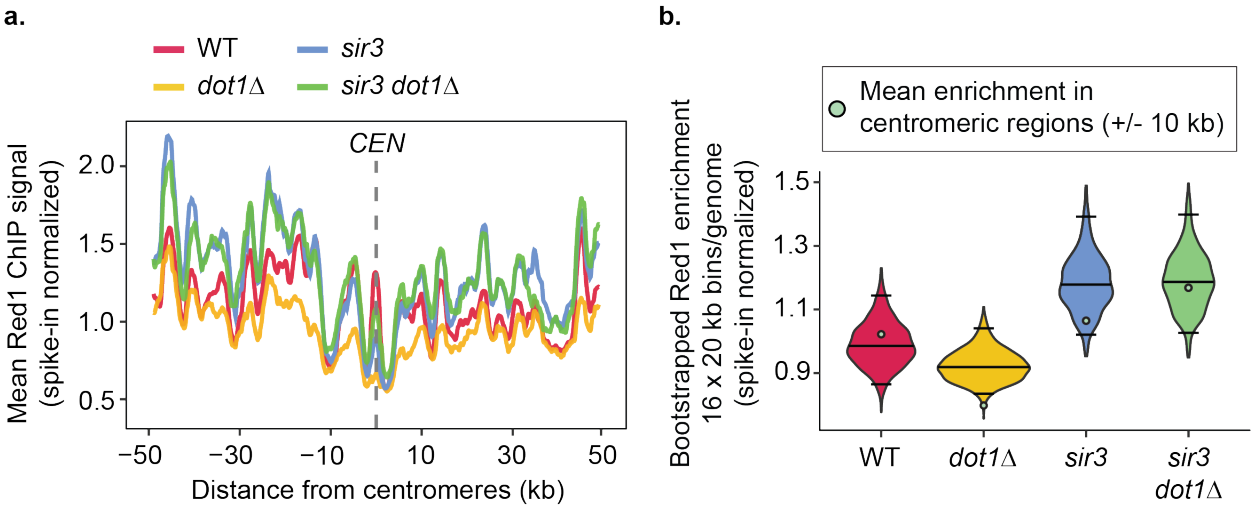

Supplementary Fig. 7: Effects of Dot1 on axis protein deposition depend on Sir3 at centromeres.

(a) Distance-from-centromere meta-profiles (±50 kb) of Red1 ChIP in WT, *dot1Δ*, *sir3*, and *sir3 dot1Δ* (spike-in normalized). WT and *dot1Δ* are from published datasets [2,3]. Dashed line marks the centromere midpoint. Signals were extracted in 100-bp bins around each centromere. **(b)** Genome-wide bootstrap distributions of fold-enrichment (16 × 20-kb windows; n = 1,000 resamples; see Methods: Bootstrapping plots). Black lines show medians and 95% CIs; orange/red circles mark the observed mean around the centromeres. Two-sided empirical test, effect sizes via Cohen's d (negative = depletion at centromeres relative to the genome-wide null): WT (p = 0.679, BH = 0.797, d = +0.43); *dot1Δ* (p = 0.020, BH = 0.080, d = −2.44); *sir3* (p = 0.186, BH = 0.372, d = −1.29); *sir3 dot1Δ* (p = 0.797, BH = 0.797, d = −0.25). All values are averages of two biological replicates and were reproducible across replicates.

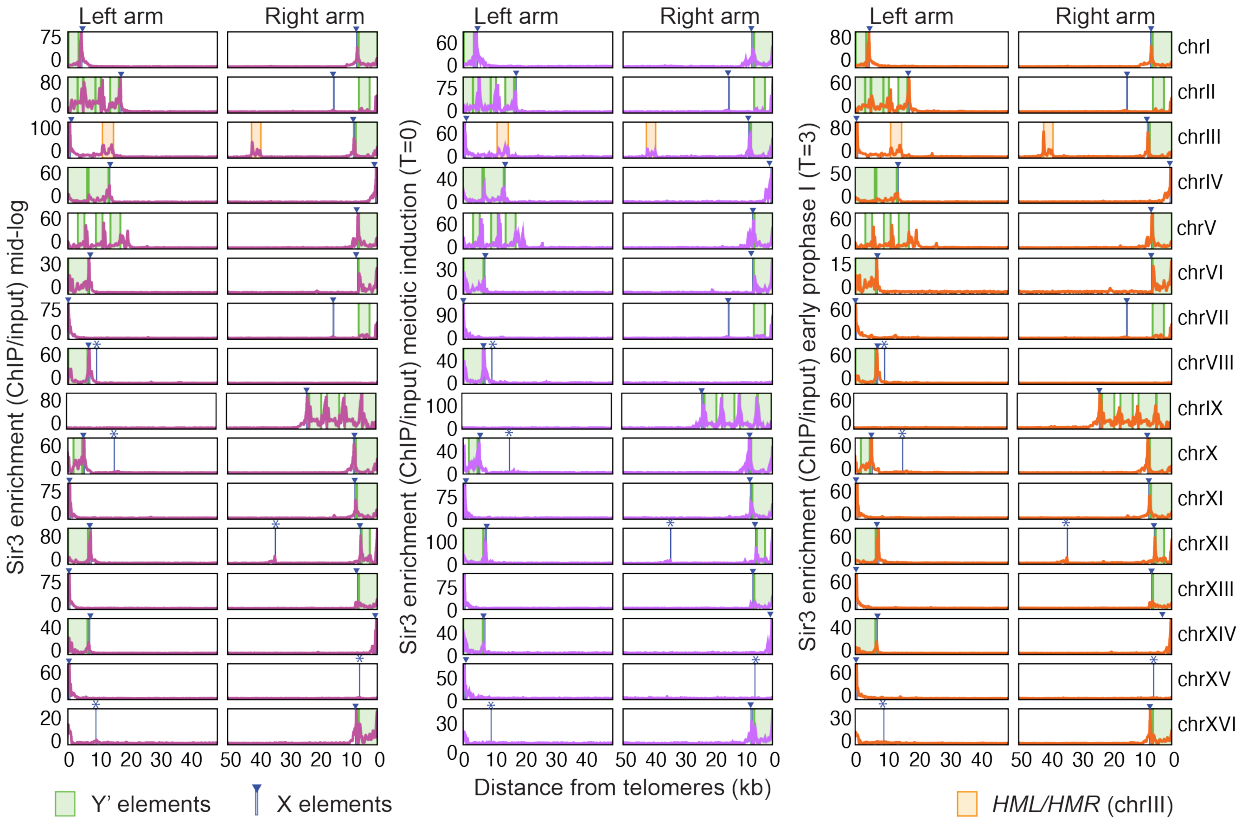

Supplementary Fig. 8: Sir3 ChIP profiles across all chromosome ends.

Distance-from-telomere Sir3 ChIP/Input signal is shown for every left and right arm (32 ends) in vegetative cells (mid-log phase), at meiotic induction (T=0), and in early prophase I (T = 3h). Green blocks mark all annotated Y′ elements and blue blocks mark X elements (fully and partially annotated copies shown: X, n = 32; Y′, n = 31). The positions of the silent mating type loci near the left (*HML*) and right (*HMR*) telomere of chrIII are also indicated. Values represent the mean of two biological replicates and were reproducible across replicates.

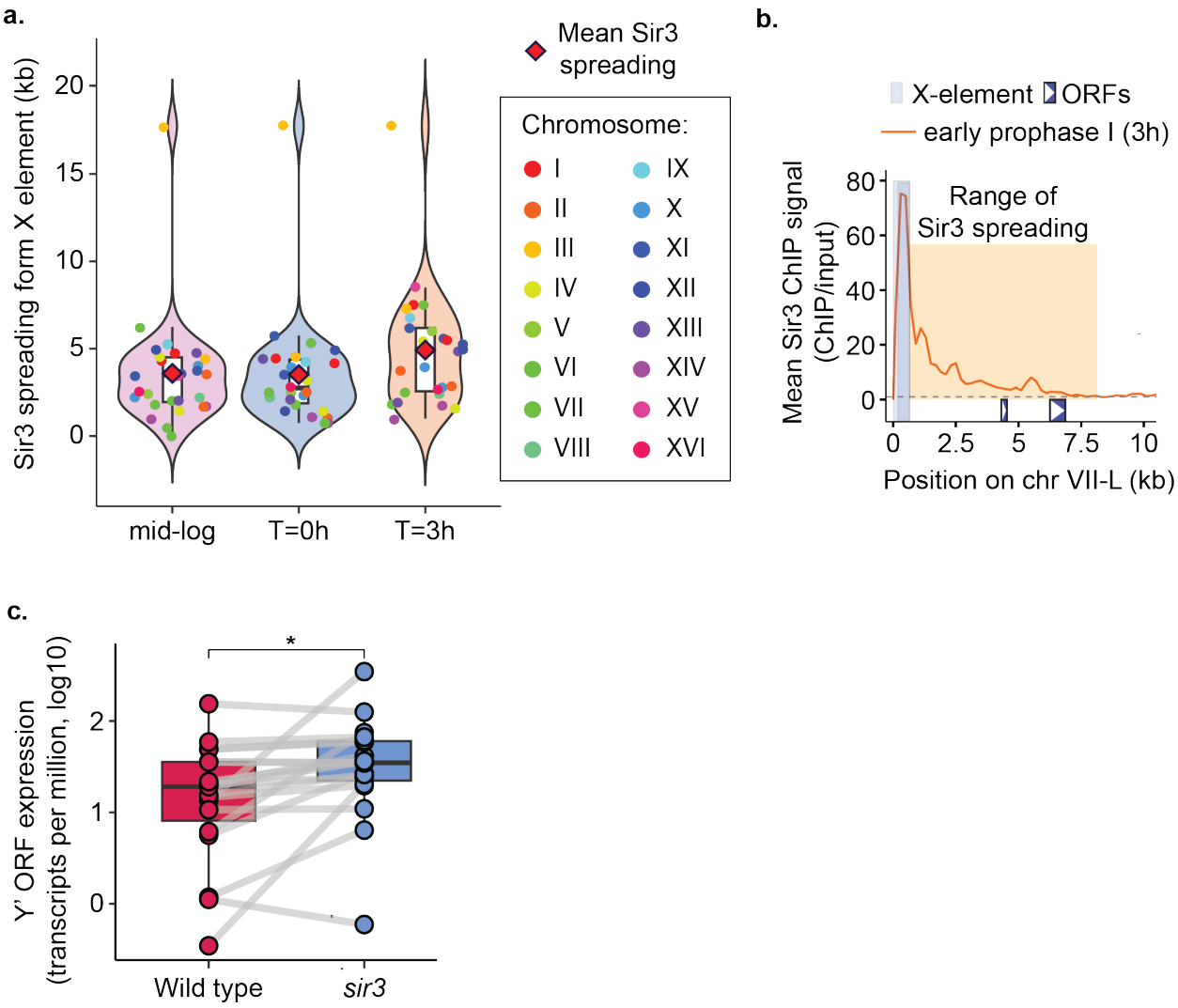

Supplementary Fig. 9: Sir3 spreading and Y′ transcription near chromosome ends.

(a) Sir3 spreading from the X element, quantified per chromosome end from Sir3 ChIP–seq (ChIP/Input) in early prophase I (see Methods: Quantification of Sir3 spreading from chromosome ends). The consistent outlier point indicates the spreading to *HML* on chr III-L. **(b)** Example illustrating the range of Sir3 spreading as quantified in (a). **(c)** Y′-element mRNA abundance at T = 3h after meiotic induction in WT and *sir3* (both *ndt80Δ*). Expression is $\log_{10}$(TPM) for annotated Y′ ORFs. Points are individual Y′ ORFs and gray lines connect the same ORF across strains. Two-sided Wilcoxon rank-sum test with rank-biserial effect size

(positive = higher in *sir3*) ($p = 0.037$, $r = 0.40$). Values represent the mean of two biological replicates and were reproducible across replicates.

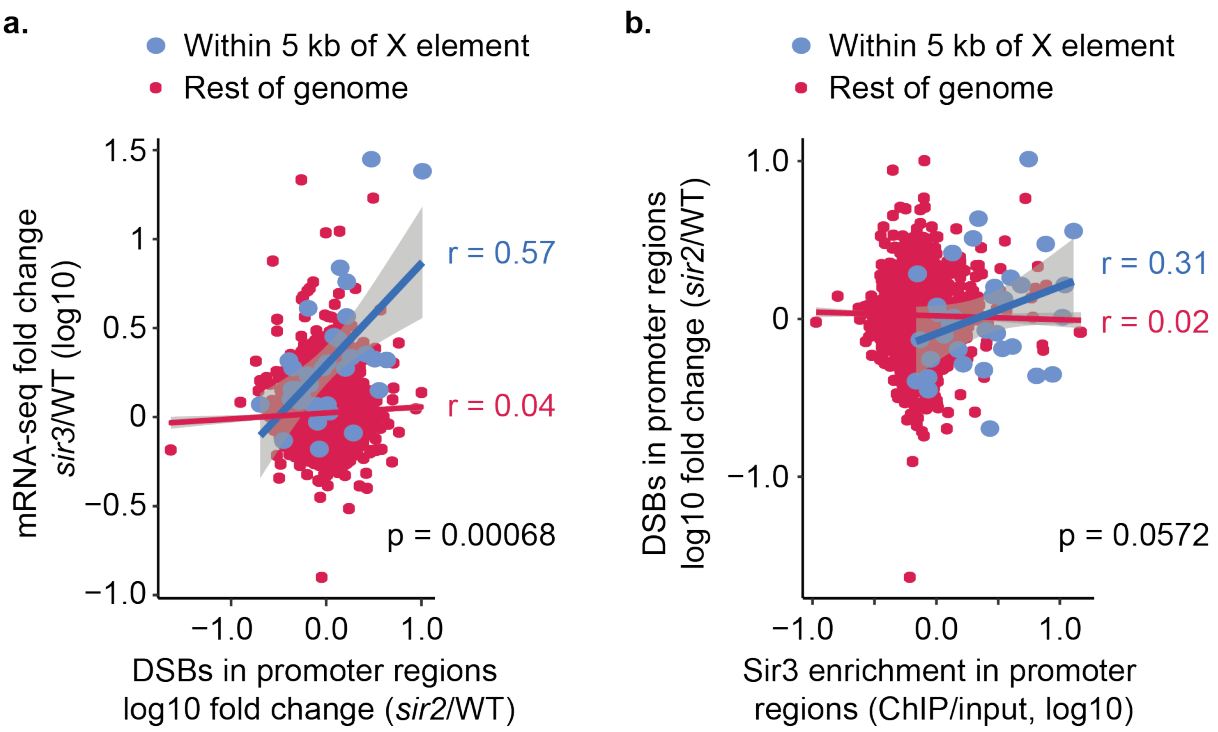

Supplementary Figure 10: Relationships among DSB changes, Sir3 occupancy, and transcription in promoters. (a) For each annotated gene, the change in Spo11-oligo signal in *sir2Δ* versus WT within the promoter (250 bp upstream of the TSS) is plotted against the change in mRNA in *sir3* versus WT ($\log_{10}$ fold change). Blue: genes within 5 kb of an X element; red: all other genes. Lines are least-squares fits with shaded 95% CIs; Pearson r values are shown. P values are based on Fisher's r-to-z transformation and two-sided z-test. Spo11 datasets are from published work [1,4] (see Methods: Promoter correlation plots). **(b)** For the same promoters, DSB change (*sir2Δ*/WT, $\log_{10}$) is plotted versus Sir3 binding in WT promoters ($\log_{10}$ ChIP/Input). Color scheme and statistics as in **(a)**.

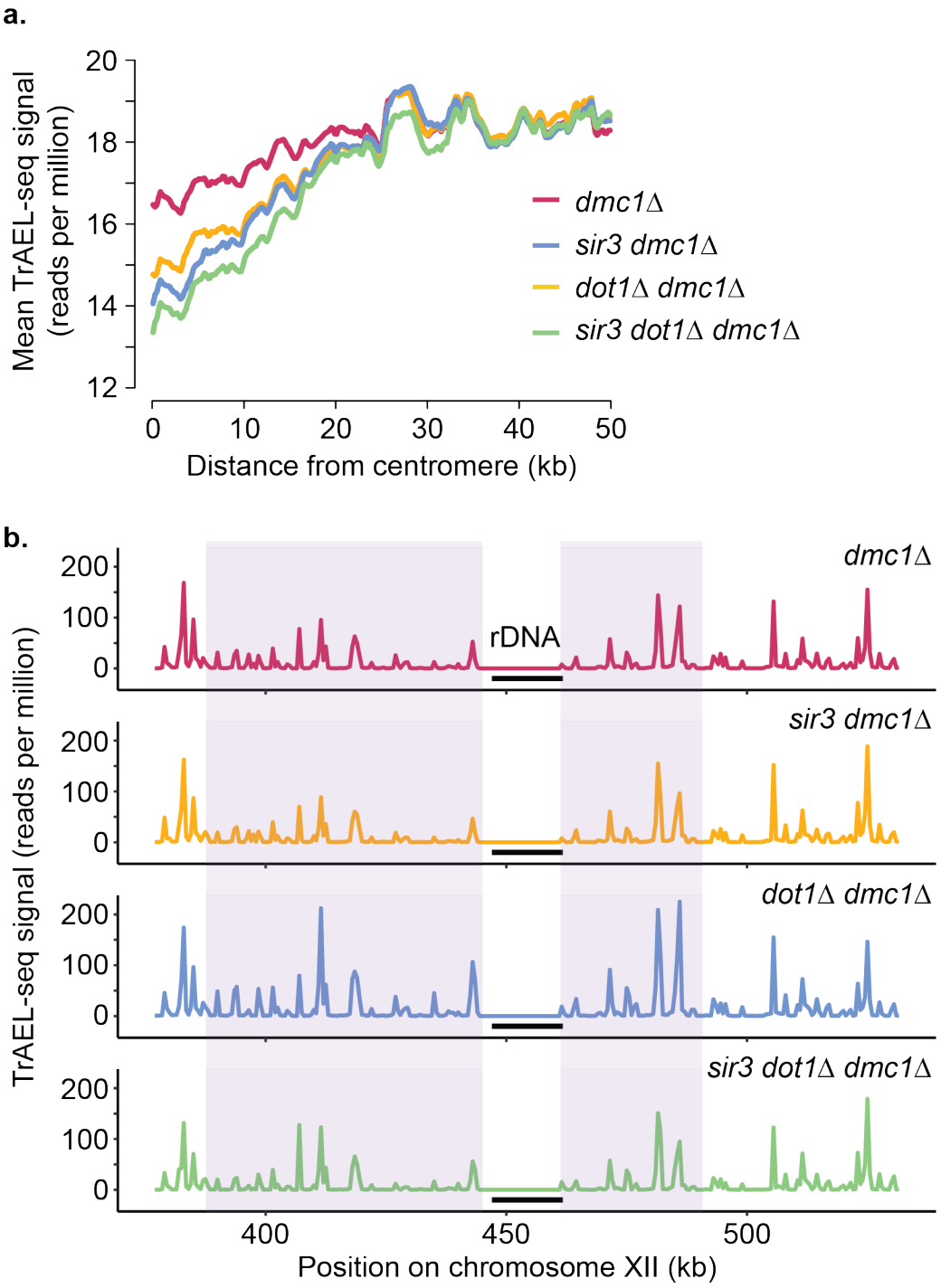

Supplementary Figure 11: Distinct and combined roles of Dot1 and Sir3 in shaping DSB landscapes around centromeres and the rDNA locus.

(a) TrAEL-seq meta-plots showing DSB signal as a function of distance from centromeres plotted for *dmc1Δ, sir3 dmc1Δ, dot1Δ dmc1Δ,* and *sir3 dot1Δ dmc1Δ* strains. Mean TrAEL-seq signal (reads per million) plotted for the four strains within ± 50 kb of centromeres. **(b)** TrAEL-seq signal versus distance from the rDNA array on chr XII; the black bar denotes the rDNA repeat region. The same four strains are shown. Purple shading marks intervals with elevated DSB signal in *dot1Δ.* Values are means of two independent biological replicates and were reproducible between replicates.

Supplementary Tables:

Supplementary Table 1: SK1 yeast strains utilized in this study

Strain number	**Genotype**
AH7797	*MATa, ho::LYS2, lys2, ura3, leu2::hisG, his3::hisG, trp1::hisG* *MATalpha, ho::LYS2, lys2, URA3, LEU2, HIS3, TRP1*
AH5217	*MATa, ho::LYS2, lys2, leu2::hisG, trp1::hisG, ura3, ARG4, his3::hisG, his4B::LEU2, dmc1Δ::ARG4* *MATalpha, ho::LYS2, lys2, leu2::hisG, TRP1, ura3, arg4-Bgl2, his4B::LEU2, dmc1Δ::ARG4*
AH3083	*MATa, ho::LYS2, lys2, leu2::hisG, his4X::LEU2-URA3, ura3, his3::hisG, trp1::hisG, arg4-Bgl2, dmc1Δ::ARG4, dot1Δ::TRP1* *MATalpha, ho::LYS2, lys2, leu2::hisG, his4B::LEU2, HIS3, trp1::hisG, ura3,arg4-nsp, dmc1Δ::ARG4, dot1Δ::TRP1*
AH2908	*MATa, ho::LYS2, lys2, leu2::hisG, his4B::LEU2, ura3, arg4-Bgl2, dmc1 Δ::ARG4, sir3::HIS3* *MATalpha, ho::LYS2, lys2, leu2::hisG, his4B::LEU2, ura3, arg4-Bgl2, dmc1Δ::ARG4, sir3::HIS3*
AH13037	*MATalpha, ho::LYS2, leu2::hisG, ura3, his4B::LEU2, trp1::hisG, dot1Δ::TRP1, arg4-Bgl2, dmc1Δ::ARG4, sir3::HIS3* *MATa, ho::LYS2, leu2::hisG, ura3, trp1::hisG, dot1Δ::TRP1, arg4-Bgl2, dmc1Δ::ARG4, sir3::HIS3*
AH8967	*MATa, ho::LYS2, lys2, ura3, LEU2, his3::hisG, trp1::hisG, sir3::HIS3, ndt80Δ::TRP1*

	MATalpha, ho::LYS2, lys2, ura3::YIplac211::URA3, LEU2, his3::hisG, trp1::hisG, sir3::HIS3, ndt80Δ::TRP1
AH6179	*MATa, ho::LYS2, lys2, HIS, URA, LEU, TRP, ndt80Δ::TRP1* *MATalpha, ho::LYS2, lys2, leu2::hisG, his4X, ura3, trp1::hisG, ndt80Δ::TRP1*
AH13257	*MATa, ho::LYS2, leu2::hisG, trp1::hisG, dot1Δ::TRP1, sir3::HIS3* *MATalpha, ho::LYS2, leu2::hisG, trp1::hisG, dot1Δ::TRP1, sir3::HIS3*
AH2861	*MATalpha, ho::LYS2, lys2, ura3, leu2::hisG, his3::hisG, trp1::hisG, sir3::HIS3* *MATa, ho::LYS2, lys2, ura3, leu2::hisG, his3::hisG, trp1::hisG, sir3::HIS3*
AH8104	*MATa, lys2, ho::LYS2, trp1::hisG, his3::hisG, LEU2, URA3, dot1Δ::TRP1* *MATalpha, lys2, ho::LYS2, trp1::hisG, HIS3, leu2::hisG, ura3, dot1Δ::TRP1*
AH13299	*MATalpha, ho::LYS2, lys2, ura3, leu2::hisG, his4X-LEU2(BamHI)-URA3, arg4-nsp, hht1-K79R, hht2-K79R* *MATa, ho::LYS2, lys2, ura3, leu2::hisG, his4B-LEU2(MluI), arg4-bgl hht1-K79R, hht2-K79R*

Supplementary Table 2: ChIP-seq datasets utilized in this study

Sample	**Time**	**Antibody**	**Type**	**GEO accession numbers**	**References**
Wild type	3 hr in meiosis	Anti-Red1	ChIP-seq	GSE69232, GSE115092	[2,3]
Wild type	3 hr in meiosis	Anti-Hop1	ChIP-seq	GSE105111	[1]
Rec8::3HA	3 hr in meiosis	Anti-HA	ChIP-seq	GSE69232	[2]

SK1 WT / S288c	3 hr in meiosis	Anti-Red1	ChIP-seq	GSE114731	[5]
S288c chrIV-chrI, *cen1Δ* /SK1 chrIV-chrI, *cen1Δ*	3 hr in meiosis	Anti-Red1	ChIP-seq	GSE114731	[5]
S288c chrIV-chrI, *cen4Δ*/SK1 chrIV-chrI, *cen4Δ*	3 hr in meiosis	Anti-Red1	ChIP-seq	GSE114731	[5]
rec8Δ	3 hr in meiosis	Anti-Red1	ChIP-seq + SNPChIP-seq	GSE156040	[6]
hop1-phd	3 hr in meiosis	Anti-Red1	ChIP-seq + SNPChIP-seq	GSE156040	[6]
hop1-phd rec8Δ	3 hr in meiosis	Anti-Red1	ChIP-seq + SNPChIP-seq	GSE156040	[6]
Wild type	4 hr in meiosis	Anti-H4K44ac	ChIP-seq	GSE59005	[7]
Wild type	4 hr in meiosis	Anti-H3K56ac	ChIP-seq	GSE59005	[7]
Wild type	4 hr in meiosis	Anti-H4	ChIP-seq	GSE59005	[7]
Wild type	4 hr in meiosis	Anti-H3	ChIP-seq	GSE59005	[7]

Wild type	4 hr in meiosis	Anti-H3K4me3	ChIP-seq	GSE67907	[8]
Wild type	3 hr in meiosis	Anti-H3K79me3	ChIP-seq	GSE287129	This study
dot1Δ	3 hr in meiosis	Anti-Red1	ChIP-seq + SNPChIP-seq	GSE115092	[2,3]
set1Δ	3 hr in meiosis	Anti-Red1	ChIP-seq + SNPChIP-seq	GSE115092	[2,3]
Wild type	Mid-log phase	Anti-Sir3	ChIP-seq	GSE287129	This study
Wild type	0 hr in meiosis (post-induction)	Anti-Sir3	ChIP-seq	GSE287129	This study
Wild type	3 hr in meiosis	Anti-Sir3	ChIP-seq	GSE287129	This study
sir3	3 hr in meiosis	Anti-Red1	ChIP-seq + SNPChIP-seq	GSE287129	This study
sir3 dot1Δ	3 hr in meiosis	Anti-Red1	ChIP-seq + SNPChIP-seq	GSE287129	This study
hht1-K79R, hht2-K79R	3 hr in meiosis	Anti-Red1	ChIP-seq + SNPChIP-seq	GSE287129	This study

Supplementary Table 3: Spo11-Oligos, RNA-seq, TrAEL-seq and MNase-seq datasets utilized in this study

Sample	**Time point**	**Methodology**	**GEO accession numbers**	**Reference**
Wild type	4 hr in meiosis	Spo11-Oligos	GSE48299	[4]
sir2Δ	4 hr in meiosis	Spo11-Oligos	GSE122882	[1]
ndt80Δ	3 hr in meiosis	RNA-seq	GSE287127	This study
sir3 ndt80Δ	3 hr in meiosis	RNA-seq	GSE287127	This study
dmc1Δ	5 hr in meiosis	TrAEL-seq	GSE287130	This study
sir3 dmc1Δ	5 hr in meiosis	TrAEL-seq	GSE287130	This study
dot1Δ dmc1Δ	5 hr in meiosis	TrAEL-seq	GSE287130	This study
sir3 dot1Δ dmc1Δ	5 hr in meiosis	TrAEL-seq	GSE287130	This study
Wild type	3 hr in meiosis	MNase-seq	GSE307629	This study
sir3	3 hr in meiosis	MNase-seq	GSE307629	This study
dot1Δ	3 hr in meiosis	MNase-seq	GSE307629	This study
sir3 dot1Δ	3 hr in meiosis	MNase-seq	GSE307629	This study

Supplementary references

1 Subramanian, V. V. *et al.* Persistent DNA-break potential near telomeres increases initiation of meiotic recombination on short chromosomes. *Nature Communications* **10**, 1-15 (2019). https://doi.org/10.1038/s41467-019-08875-x

2 Sun, X. *et al.* Transcription dynamically patterns the meiotic chromosome-axis interface. *eLife* **4**, 1-23 (2015). https://doi.org/10.7554/eLife.07424

3 Vale-Silva, L. A., Markowitz, T. E. & Hochwagen, A. SNP-ChIP: A versatile and tag-free method to quantify changes in protein binding across the genome. *BMC Genomics* **20**, 1-10 (2019). https://doi.org/10.1186/s12864-018-5368-4

4 Thacker, D., Mohibullah, N., Zhu, X. & Keeney, S. Homologue engagement controls meiotic DNA break number and distribution. *Nature* **510**, 241-246 (2014). https://doi.org/10.1038/nature13120

5 Luo, J. *et al.* Synthetic chromosome fusion: Effects on mitotic and meiotic genome structure and function. *Cell Genomics* **3** (2023). https://doi.org/10.1016/j.xgen.2023.100439

6 Heldrich, J. *et al.* Two pathways drive meiotic chromosome axis assembly in *Saccharomyces cerevisiae*. *Nucleic Acids Research* **50**, 4545-4556 (2022).

7 Hu, J. *et al.* H4K44 Acetylation Facilitates Chromatin Accessibility during Meiosis. *Cell Reports* **13**, 1772-1780 (2015). https://doi.org/10.1016/j.celrep.2015.10.070

8 Zhu, X. & Keeney, S. High-resolution global analysis of the influences of Bas1 and Ino4 transcription factors on meiotic DNA break distributions in *Saccharomyces cerevisiae*. *Genetics* **201**, 525-542 (2015). https://doi.org/10.1534/genetics.115.178293